EES Batteries

ROYAL SOCIETY OF CHEMISTRY

REVIEW

View Article Online
View Journal | View Issue

Cite this: *EES Batteries*, 2025, **1**, 364

Insights into chemical substitution of metal halide solid-state electrolytes for all-solid-state lithium batteries

Chao Wu, [a] Zhen Wang, [a] Zhanhui Jia,[b] Jiawu Cui,[a] Chengyong Shu,[a] Xiaowei Wang, *[c] Yuping Wu [d] and Wei Tang *[a]

Over a long period of time, frequent safety incidents in electric vehicles and portable electronics have raised concerns about modern energy storage devices, particularly lithium-ion batteries. However, the emergence of solid-state electrolytes (SSEs) with good thermal stability has eliminated potential safety hazards of conventional lithium-ion batteries, such as liquid electrolyte leakage and explosions, allowing all-solid-state batteries to attract intensive attention. Among all types of SSEs, halide SSEs have gained research focus owing to their high ionic conductivity, good mechanical malleability, and excellent chemical/electrochemical stability. They have risen to the forefront of SSE research within just a few years. This paper firstly summarizes state-of-the-art halide SSEs by briefly introducing various synthesis methods of halide SSEs and comparing their advantages and disadvantages. Secondly, it introduces the composition, structural types, and ionic conduction mechanisms of halide SSEs, analyzing their effects on ionic transport behavior mainly from three perspectives: anion polarizability, cation disorder and stacking faults. Primarily, it not only reviews typical substitution types for current halide SSEs, explaining how each type optimizes ion transport kinetics, but also focuses on chemical substitution strategies to improve the inherent thermodynamic stability window of halide SSEs and the complex electrode/SSE interface. Additionally, this work proposes potential future research directions to address the challenges in the development of halide SSEs. Overall, the review aims to provide fundamental understanding for designing new halide SSEs and their structural characterization.

Received 20th January 2025,
Accepted 28th February 2025

DOI: 10.1039/d5eb00010f

rsc.li/EESBatteries

Broader context

Given the increasing global demand for clean energy and efficient energy storage technologies, the development of all-solid-state lithium-ion batteries (ASSLBs) with excellent performance and high safety has become a hot topic in scientific research. In particular, the research on solid-state electrolytes (SSEs) has become critical to achieve higher energy density, longer cycle life and wider operating temperature range. In recent years, halide SSEs have attracted much attention due to their outstanding physicochemical properties. High room-temperature ionic conductivity implies fast lithium-ion transport kinetics, and good chemical stability and mechanical strength guarantee battery safety. In this review, the current research status on halide SSEs and the diverse synthesis methods are first briefly described. Next, the basic structural framework and ion transport mechanism of halide SSEs are outlined, and the factors affecting the ion transport behavior are summarized. It then focuses on chemical substitution and explores the specific mechanisms by which it enhances lithium-ion transport kinetics and improves the stability of the electrode/SSE interface by optimizing the electrolyte structure and composition. In addition, this paper also proposes key breakthrough directions for future halide SSEs, which is expected to provide a more solid theoretical foundation for subsequent research work.

1. Introduction

As the energy storage market evolves, all-solid-state lithium-ion batteries (ASSLBs) are gradually replacing traditional liquid lithium-ion batteries, becoming the cornerstone of large-scale energy storage systems. These batteries address the growing demand for high-energy and high-power storage in power grids and public utilities. The primary advantage of ASSLBs lies in their potential to surpass the energy density limits of

[a]*School of Chemical Engineering and Technology, Xi'an Jiaotong University, Xi'an, 710049, China. E-mail: tangw2018@xjtu.edu.cn*
[b]*School of Materials Science and Engineering, Xi'an Jiaotong University, Xi'an, 710049, China*
[c]*Chemical Sciences and Engineering Division, Argonne National Laboratory, Lemont, IL, 60439, USA. E-mail: xiaowei.wang@anl.gov*
[d]*School of Energy and Environment, Southeast University, Nanjing 210096, China*

liquid lithium-ion batteries, aiming for a high energy density of 500 Wh kg^{-1}.[1–4] Additionally, the use of solid-state electrolytes (SSEs) with strong thermal stability eliminates the safety risks, such as thermal runaway and explosions, associated with flammable organic electrolytes. SSEs, a critical component of ASSLBs, have been extensively researched and come in various forms, including polymers, oxides, sulfides and halides. Generally, polymeric SSEs, including poly(ethylene oxide) (PEO), poly(vinylidene fluoride) (PVDF), polyacrylonitrile (PAN), and poly(methyl methacrylate) (PMMA), exhibit better mechanical flexibility, lower mass density, and straightforward synthesis methods. However, their intrinsic ionic conductivity is slow, which is commonly addressed by incorporating ceramic fillers, ionic liquids or metal–organic frameworks (MOFs) to form composite polymeric SSEs.[5–9] Oxide SSEs provide good environmental and electrochemical oxidation stability but require high sintering temperatures (over 1000 °C) and lack flexibility, resulting in high fabrication costs.[10,11] Sulfide SSEs boast high ionic conductivity with excellent mechanical machinability, but they are highly sensitive to water, producing toxic H_2S gas upon hydrolysis, which quickly deteriorates their ionic conductivity.[12–14] Additionally, their poor electrochemical oxidation stability limits compatibility with conventional 4 V cathode materials. In contrast, halide SSEs have garnered significant attention in ASSLBs research owing to their high ionic conductivity (~10^{-3} S cm^{-1}) at room temperature (RT), wide electrochemical stability window, excellent environmental tolerance and diverse synthetic routes.[15–17] These properties allow halide SSEs to overcome many limitations of other SSEs.

The development of halide SSEs has undergone significant changes, as illustrated in Fig. 1, which highlights key milestones chronologically. Generally, the evolution of halide SSEs can be divided into two phases, with a pivotal shift occurring in 2018. Before 2018, halide SSEs were held back by their low ionic conductivity, which limited their potential for practical use. At the same time, SSEs like oxides and sulfides were advancing rapidly, causing halide SSEs to attract less interest and resulting in minimal experimental and theoretical exploration during this period. However, a breakthrough came in 2018 when Asano *et al.* successfully synthesized two halide SSEs with high ionic conductivity, *i.e.*, Li_3YCl_6 (5.1×10^{-4} S cm^{-1}) and Li_3YBr_6 (1.7×10^{-3} S cm^{-1}).[22] This marked a major milestone in halide SSEs development, as it was the first time their ionic conductivity surpassed the 1×10^{-3} S cm^{-1} threshold. Following this discovery, research interest in halide SSEs surged, leading to the development of various high-ionic-conductivity halide SSEs in just five to six years, such as Li_3AlF_6, Li_3GaF_6, Li_3InCl_6, Li_3ScCl_6, Li_3ErCl_6, $Li_2Sc_{2/3}Cl_4$, Li_3HoBr_6 and Li_3ErI_6.[25,36–42] More importantly, given that all constituent elements of ternary halide SSEs are exchangeable, the structure and chemical composition of the halide SSEs family have been greatly enriched by chemical substitution of elements, *e.g.*, $Li_{3-x}M_{1-x}Zr_xCl_6$ (M = Er/Y), $Li_{2+x}Zr_{1-x}Fe_xCl_6$ ($0 \leq x \leq 0.5$), $Li_3Y_{1-x}In_xCl_6$ ($0 \leq x \leq 1$), $Li_3YBr_3Cl_3$ and $Li_3InCl_{4.8}F_{1.2}$.[26,28,29,43,44] These substituted halide SSEs surprisingly demonstrate significantly improved ionic conductivity compared with their original counterparts.

It is important to note that halide SSEs encounter interfacial challenges similar to those observed in other SSEs, including significant interfacial side reactions, inadequate interfacial contact and the formation of space charge layers, all of which hinder their further advancement.[45,46] To tackle these issues, two well-established interface modification strategies have been extensively explored. The first involves the application of functional coatings (*e.g.*, LiF, Li_3PO_4) onto the surface of halide SSEs, which serves to mitigate interfacial side reactions and lower interfacial impedance.[47–49] The other strategy focuses on the design of nanostructured architectures or the incorporation of a flexible interfacial layer on the halide SSEs surface, effectively improving the physical contact between halide SSEs and electrodes.[50–53] Nevertheless, these

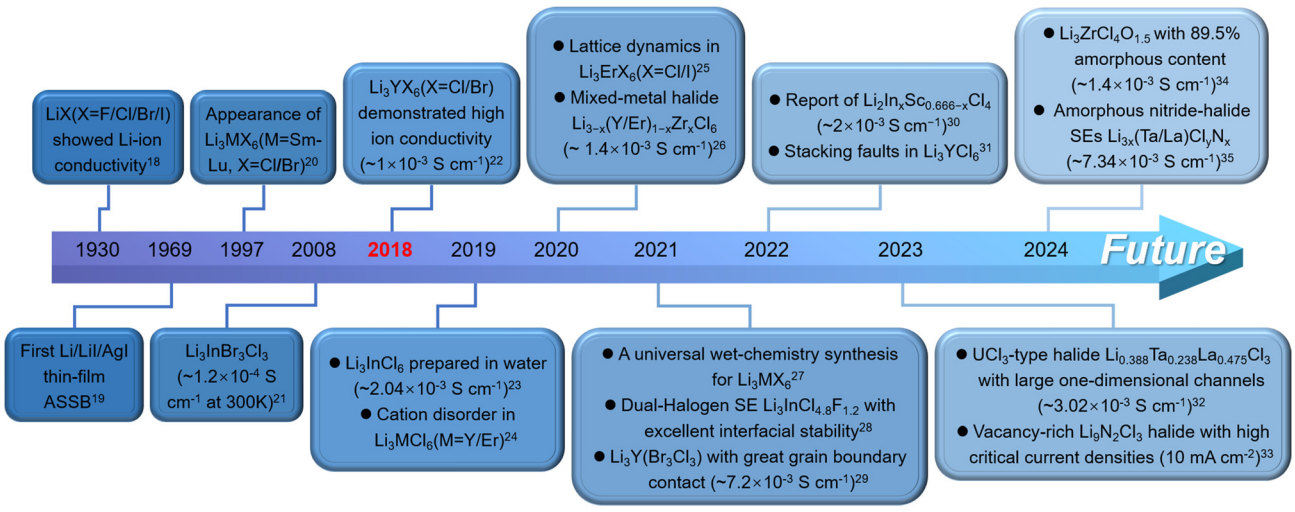

Fig. 1 The development history of halide SSEs for ASSLBs with representative achievements.[18–35]

approaches fail to address the intrinsic electrochemical stability of halide SSEs. To achieve significant interface modification, it remains crucial to modify the surface chemistry of halide SSEs through chemical substitution. Specifically, anionic substitution can regulate the reactivity of the halide SSEs' surface, thereby facilitating the formation of a stable interface with the electrode. Furthermore, the chemical substitution strategy helps optimize the mechanical properties of halide SSEs, thereby minimizing the formation of cracks.

The synthetic strategies of halide SSEs have also been widely discussed in recent years. Each synthesis route features unique operating conditions and processing parameters that influence the crystal structure and ionic transport behavior of halide SSEs, ultimately affecting the electrochemical properties of ASSLBs. Currently, the most widely used synthesis method is mechanical ball milling, which requires precise control over milling time and speed.[15,17] In this process, the mechanical energy generated during high-energy ball milling is converted into the activation energy needed for precursor chemical reactions, resulting in metastable halide SSEs with low crystallinity. Alternatively, solid-phase sintering can be used to increase the crystallinity of halide SSEs and achieve a more stable structure. This method involves sealing the precursor in a vacuumed quartz tube and continuously heating it at elevated temperatures (typically above 350 °C). However, both ball milling and solid-phase sintering are energy-intensive and time-consuming processes, often producing samples that are not homogeneous and that can form impurity phases due to element volatilization at high temperatures. Therefore, it is imperative to explore the liquid phase synthesis methods with mild reaction conditions and high-purity products. A pioneering study by Li *et al.* demonstrated the first aqueous synthesis of halide SSEs through the production of Li_3InCl_6.[23] In this process, raw materials were dissolved in water, naturally dried in air to form $Li_3InCl_6{\cdot}H_2O$, and then heated in a dynamic vacuum at 100–200 °C for 4 hours to produce high-purity Li_3InCl_6. Since then, several liquid-phase synthesis methods have been developed, such as ammonium-assisted wet chemistry, vacuum evaporation-assisted synthesis, ethanol-mediated Li_3InCl_6 synthesis and freeze-drying techniques.[27,54–56] The liquid-phase synthesis method, while offering significant advantages in terms of material homogeneity, controlling the microscopic morphology or size of SSEs, and fabricating electrode sheets, is more complex and costly. More importantly, it imposes higher requirements on the humidity tolerance of the precursor. Therefore, current research on liquid-phase synthesis primarily focuses on Li_3InCl_6. As such, there is still considerable progress needed before this method can be widely applied.

This review underscores the most recent progress in the realm of halide SSEs and provides a comprehensive understanding of the structure–property relationship for halide SSEs through the lens of chemical substitution. By systematically analyzing the effects of chemical substitution on ionic conductivity and interfacial stability, it elucidates the fundamental linkages between diverse substitution mechanisms and the electrochemical performance of materials, thereby establishing a more resilient analytical framework. Moreover, this study outlines promising avenues for future research on chemical substitution strategies in halide SSEs, encompassing high-throughput screening of substitutional elements and the design of novel halide SSEs driven by machine learning. These insights offer a forward-thinking perspective that can steer the ongoing development and refinement of halide SSEs, with the objective of rapidly increasing their market share in the commercial landscape of ASSLBs.

2. Structure and ion transport in halide SSEs

2.1 Structural composition

The general formula of ternary halide SSEs is Li_aMX_b (M = Y, Sc, In, La–Lu, *etc.*, X = F, Cl, Br, I), which is a completely new crystal structure formed by doping rare-earth element M based on LiX structure. Since the ionic radii of the halogen elements are larger than those of almost all rare-earth elements, so the ternary halide SSEs take the anion close-packed sublattice as the basic framework. Among them, the radii and polarity of cations and anions have a remarkable effect on the crystal structure. According to the Pauling coordination polyhedron rule, close contact of cations and anions is the prerequisite for the stabilization of crystal structures. Hence, Liang *et al.* generalized the structures of all halide SSEs and innovatively proposed to classify the crystal structures by using the radius ratio of M cation to X anion (r^+/r^-), marked as $t_{m/x}$.[57]

For the currently dominant Li_3MX_6 and Li_2MX_4-type SSEs, t = 0.732–0.414, the anion sublattice can be partitioned into hexagonal close packing (hcp) and cubic close packing (ccp), as shown in the Fig. 2.[58] Further refinement of these two sublattices based on the t values leads to two conclusions: (1) when t = 0.637–0.599, the close-packed anions are stacked in ABAB mode. Due to the different symmetric distributions of Li^+ and non-Li^+ cations on the octahedral (Oct) sites, trigonal (space group: $P\bar{3}m1$) and orthorhombic (space group: *Pnma*) structures are formed, such as Li_3YCl_6 and Li_3YbCl_6.[22,59,60] (2) With t value decreases, the close-packed anions are stacked in ABCABC mode. Given the difference in cation occupancy, monoclinic structures (space group: $C2/m$) and spinel structures (space group: $Fd\bar{3}m$) are formed, such as Li_3InCl_6 and Li_2MgCl_4.[38,61]

Furthermore, the rare-earth halide UCl_3 (U = La–Sm), featuring a non-close-packed anion lattice, exhibits a unique and fascinating structural framework.[32,62,63] In contrast to conventional halide SSEs, the metal cations in UCl_3-type structures (space group: $P6_3/m$) adopt ninefold coordination, forming tricapped trigonal prismatic polyhedra. This high-coordination-number structure not only stabilizes the metal cations but also generates abundant one-dimensional Lithium-ion migration pathways.[64,65] Consequently, UCl_3-type materials are widely acknowledged as promising contenders for lithium superionic

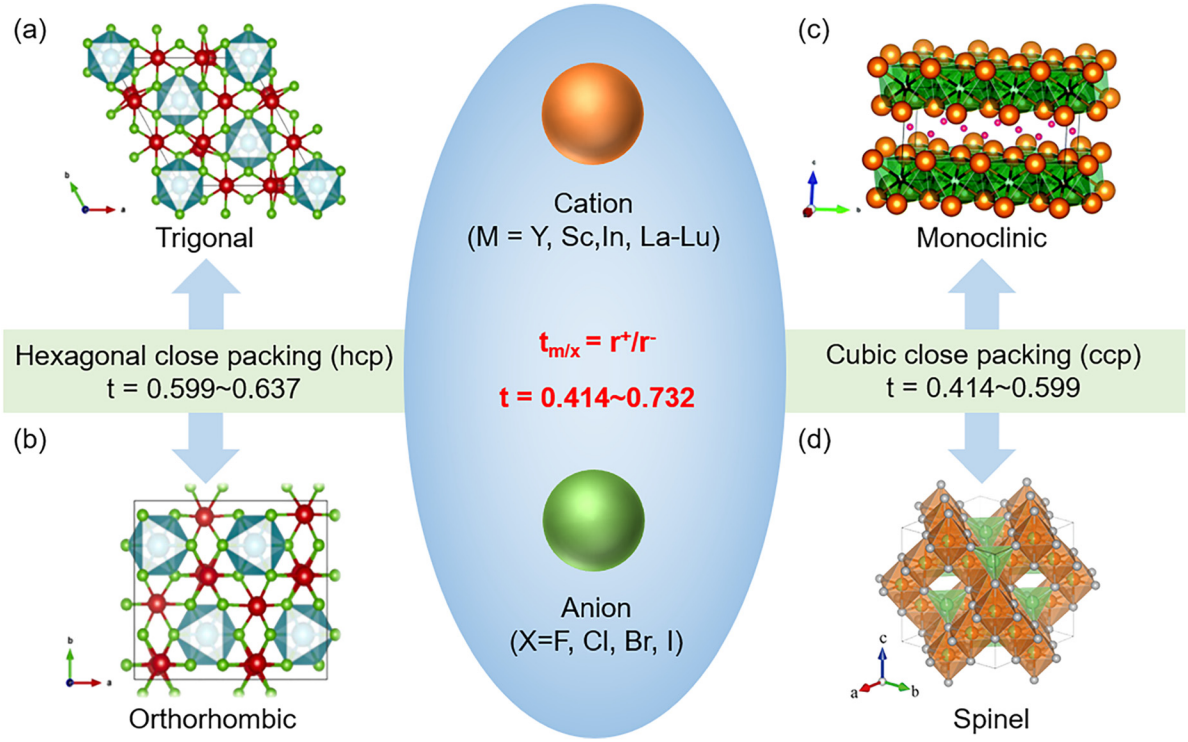

Fig. 2 Common crystal structures of halide SSEs. (a) Trigonal structure. (b) Orthorhombic structure. Reproduced with permissions from ref. 60. Copyright 2021, Elsevier. (c) Monoclinic structure. Reproduced with permissions from ref. 38. Copyright 2019, The Royal Society of Chemistry. (d) Spinel structure. Reproduced with permissions from ref. 61. Copyright 2024, American Chemical Society.

conductors, holding substantial potential for advanced ASSLBs applications.

2.2 Li^+ conduction mechanism

Li^+ migration in halide SSEs is realized by hopping motion, and the hopping sites of Li^+ depend on the type of the anion sublattice, resulting in different migration pathways.[22,66] For the hcp structure, Li^+ hops among adjacent face-sharing Oct sites (Oct–Oct) along the *c*-axis, forming rapid diffusion 1D channels, whereas in the *ab* plane, there exist vast tetrahedral (Tet) interstitial sites, which lie between the two edge-sharing octahedra. They connect all the 1D channels (Oct–Tet–Oct) and a 3D anisotropic diffusion network is ultimately formed (Fig. 3a). However, Li^+ migration in these 1D fast channels is prone to be blocked, resulting in ionic conductivities lower than the theoretically calculated values. For the ccp structure, Li^+ migration between different Oct sites along all directions requires the assistance of Tet interstitial sites (Oct–Tet–Oct), yielding a 3D isotropic diffusion network (Fig. 3b), which is similar to the migration path along the *ab* plane in the hcp structure. For the two ccp structures, the Oct sites for Li^+ hopping are usually occupied by non-lithium cations in the spinel structure, which also hinders the diffusion of Li^+.[16] Therefore, the monoclinic phase structure may be the most favorable structure for Li^+ migration in halide SSEs, which has also been demonstrated by experiments and theoretical calculations.[39,59,67]

In addition to the long-range diffusion characteristics, short-range diffusion caused by defects (vacancies and interstitial sites) also affects the migration behavior of Li^+. The possibility of carriers jumping between neighboring Octahedral sites depends on the content of the surrounding active Li^+ and vacancy concentrations. As suggested by Famprikis *et al.*, the diffusion mechanism mediated by vacancy clusters is the main ionic conduction mechanism.[68] Higher vacancy concentration and lower adjacent Li^+ content would be more favorable for Li^+ transport. Van Der Ven has calculated the migration barriers of Li^+ in different close-packed lattices (Fig. 3d and e), which confirmed the increase of vacancies number around the Tet interstitial sites favors the reduction of the Li^+ migration barrier.[69] Although this migration pathway requires passing through Tet interstitial sites, it provides the flattest energy landscape. For Li_3MX_6-type, M^{3+} replaces Li^+ at three Oct sites, and two vacancies are created based on charge balance. Among all Oct sites of the anion sublattice, the ratio of Li^+, M^{3+}, vacancies is 3 : 1 : 2. Therefore, the vacancies occupy 33% of the Oct sites, providing vast available hopping sites for Li^+, which is necessary to achieve high ionic conductivity.[15,70]

Indeed, the realization of ions' hopping motion between different sites requires overcoming the inter-site energy difference, which is related to the occupation of ions in the surrounding sites. It should be noted that the Tetrahedral interstitial sites act as the bridge in ionic conduction of halide SSEs. When their adjacent Octahedral sites are occupied only by Li^+

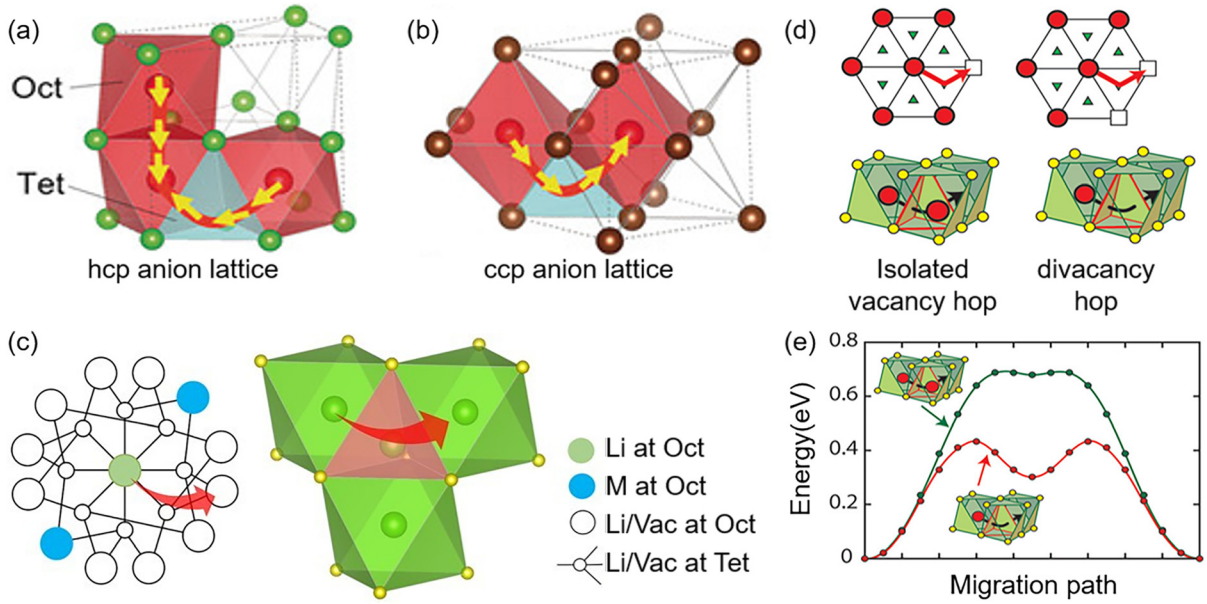

Fig. 3 (a and b) The Li-ion migration pathways in hcp anion lattice and ccp anion lattice. Reproduced with permissions from ref. 66. Copyright 2019, Wiley-VCH. (c) The schematic of the "Li-rich" environment. Reproduced with permissions from ref. 71. Copyright 2022, Elsevier. (d and e) Li^+ diffusion and corresponding energy barriers in close-packed anion sublattice by vacancy clusters (divacancies in the layered form). Reproduced with permissions from ref. 69. Copyright 2012, American Chemical Society.

or vacancies, this prevents strong electrostatic interactions between cations and narrows the energy difference between sites.[71] Then the "Li-rich" environment is formed (Fig. 3c). In addition, differences in Li^+ concentration and cation configuration are also responsible for the different ionic conductivity. Mo *et al.* systematically studied a sequence of halide SSEs through *ab initio* molecular dynamics (AIMD) simulations and concluded that low Li^+ content (approximately 40–60%), sparse cation arrangement, and low cation concentration make ion migration easier.[72]

2.3 Factors affecting ion migration dynamics

In addition to the migration pathways mentioned above, ion transport kinetics can also be affected by many factors, including lattice dynamics, cation disorder, and stacking faults, *etc.*

Lattice dynamics refers to the vibrations of crystal atoms at equilibrium positions, which affects the magnitude of the activation barriers for ion migration.[57] Reduction of Li^+ vibrational frequency contributes to enhancement of fast Li^+ transport performance. This can be explained by the softness of the anion structural frameworks. When the more polarized anion is bound to Li^+, the binding effect of Li^+ during the migration is weakened due to the longer bond lengths, *i.e.*, a lower Li^+ vibrational frequency is obtained (Fig. 4a), which leads to a higher ionic conductivity.[25] Therefore, superionic conductors tend to possess low Li^+ vibrational frequencies, and their distinctive structural features are expressed as softer and more polarized anion sublattices.[40,73,74] As shown in Fig. 4b, by replacing all the anions in Li_3ErCl_6 with the more polarizable I^-, the polarization of the anion sublattice was elevated, obtaining the lower activation barrier and higher ionic conductivity. However, with the addition of more polarizable anions, the average vibrational frequency of the anion phonon band centers was also degraded and the electrochemical oxidation stability started to deteriorate (Fig. 4c).[75] Muy attributed this phenomenon to the reaction kinetics, arguing that the reduction in vibrational frequency of the phonon band centers diminished the anion migration enthalpy and facilitated the oxidation reaction.[76] Consequently, it is necessary to balance the ionic conductivity and electrochemical stability when probing new Lithium-ion conductors.

In halide SSEs systems with the same composition, cation order–disordered arrangement can be caused by changing the synthesis method and annealing temperature. Samples typically synthesized using mechanochemical methods have higher cation disorder, favoring the formation of migration channels with flat energy landscapes.[77,78] This was also confirmed by Schlem *et al.* on the arrangement of cation sites in Li_3MCl_6 (M = Er/Y).[24] They found that Li_3MCl_6 prepared by high-energy ball milling has the highest degree of cation disorder between the Er/Y sites (Fig. 4e), *i.e.*, many M2 sites are swapped to M3 sites. High M2–M3 disorder caused the change of the repulsion force against the surrounding Li^+, prompting Li^+ sublattice rearrangement (Fig. 4d), which dramatically reduced the energy barrier for Li^+ migration along the *c*-axis. At the same time, the reordered cation sublattices also led to local structural distortions, which benefited the increase of the polyhedral transition areas and the expansion of the bottlenecks for Li^+ migration. A similar phenomenon was observed in the study of Ito *et al.*, where β-Li_3YCl_6 with more disordered

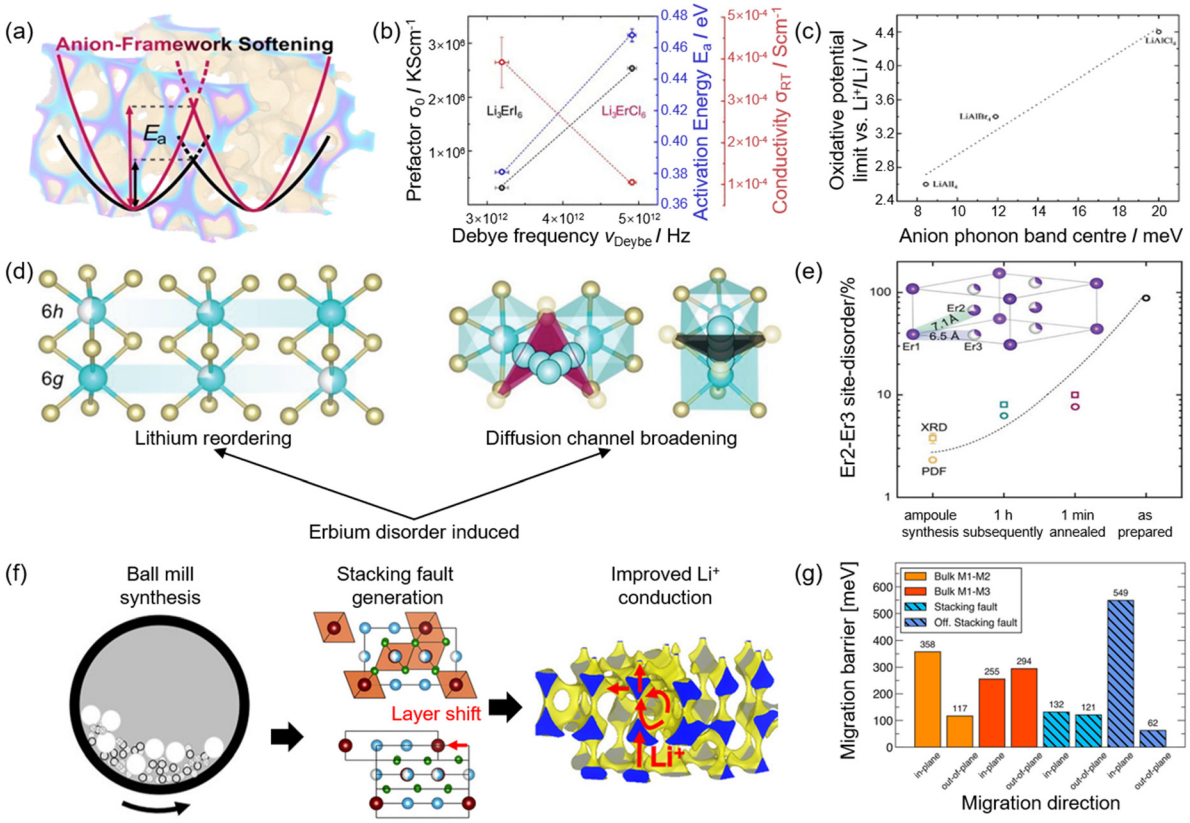

Fig. 4 Factors affecting Li-ion transport behavior. (a) The diagram of anion polarizability affecting the activation barrier by changing the ion vibrational frequency. (b) Plots of σ_0, E_a and σ as a function of the Debye frequency for Li_3ErX_6 (X = Cl, I). Reproduced with permissions from ref. 25. Copyright 2020, American Chemical Society. (c) Correlation curves of the oxidative potential limit with the anion phonon band centre for $LiAlX_4$ (X = Cl, Br, I). Reproduced with permissions from ref. 75. Copyright 2022, The Royal Society of Chemistry. (d) Influence of cation disorder on crystal structure. (e) Change of the Er2–Er3 disorder as revealed by Rietveld refinements (open squares) and G(r) fits (open circles). Reproduced with permissions from ref. 24. Copyright 2019, Wiley-VCH. (f) Schematic diagram of stacking faults. (g) Predicted Li^+ migration barriers in four model structures. Reproduced with permissions from ref. 31. Copyright 2022, American Chemical Society.

Y^{3+} sublattice exhibited stronger ion transport behavior compared with α-Li_3YCl_6.[79] Overall, cation sites' disorder in the crystal structure affects the arrangement of Li^+ sites, volume changes and local distortions of the polyhedral, thus modifying the Li^+ migration path and ionic conductivity.

Consistent with most layered oxide cathodes, stacking faults may be prevalent in halide SSEs. However, the correlation between stacking faults and ion transport was not effectively demonstrated until 2022, when Sebti *et al.* first demonstrated the presence of stacking faults in Li_3YCl_6, by using high-resolution synchrotron X-ray diffraction and DFT calculations, which optimized Li^+ conduction by generating additional interlayer channels for Li^+ migration and lowering the migration barrier (Fig. 4f).[31] Specifically, these planar defects altered the distribution of Y^{3+}, forming face-shared YCl_6^{3-} octahedra and other sparse Y^{3+} distribution regions. The presence of stronger Coulomb repulsion near these YCl_6^{3-} octahedra made the Li^+ diffusion channel along the *c*-axis locally disconnected, whereas these disconnected Li sites were reconnected by loops to form the new diffusion channel with lower migration barriers. And in the sparse Y^{3+} distribution area, Li^+ were subject to weakened Coulomb repulsion by Y^{3+} and the migration barrier was reduced. Fig. 4g shows the Li^+ migration barriers predicted by the four different models, and it could be found that the stacking fault model had the smallest migration barriers. This provided important data support for the fact that high concentration stacking faults can boost the Li^+ migration in Li_3YCl_6. It is worth mentioning that samples synthesized by mechanochemical methods tend to exhibit both stacking faults and cation disorder due to the lower energy required for the occurrence of stacking faults.[80,81]

In addition, the blocking effect of M^{3+}, grain boundaries and impurities have also been shown to be important factors affecting ion migration.[29,39,82] Only comprehensive consideration of the influence mechanisms of all factors can help us understand ion migration more deeply.

3. Enhanced ion transport by chemical substitution

To date, although Li_3ScCl_6 exhibits the highest ionic conductivity ($\sigma = 3 \times 10^{-3}$ S cm^{-1}) among all ternary halide SSEs, it is still not comparable to the excellent ionic transport properties

of conventional organic electrolytes.[39] In order to facilitate the practical application of halide SSEs, chemical substitution is considered to be an effective method to enhance ionic conductivity, which optimizes the components through elements with different charges and radii to influence the structural framework and vacancy concentration. Table 1 summarizes the crystal structure and ionic conductivity changes of typical halide SSEs before and after various chemical substitutions. Chemical substitution can be categorized into three categories: (1) aliovalent cation substitution; (2) isovalent cation substitution; (3) anion substitution. It is worth noting that the influence of each substitution type on the ion transport mechanism is completely different and will be discussed in detail below.

3.1 Aliovalent cation substitution

The enhancement of the Lithium-ion transport properties in halide SSEs by aliovalent substitution cannot be separated from many factors. In addition to the increase in vacancy concentration due to the introduction of aliovalent cations, changes in Li^+ concentration and distribution as well as the evolution of the local structural framework are also crucial. For trivalent metal halides, tetravalent Zr^{4+} and Hf^{4+} are often used as aliovalent cations.[26,85,93,103,104] Because of their abundant reserves, low cost, suitable sizes and good redox stability, they are expected to achieve large-scale commercial application of halide SSEs.

As the packing style of the anion sublattice depends on the cation–anion radius ratio, aliovalent substitution leads to the transformation of the crystal structure or rearrangement of the Li^+ sublattice, which results in a significant change for the carrier diffusion path. Park *et al.* successfully achieved structural modulation and ionic conductivity enhancement by introducing Zr^{4+} into Li_3MCl_6 (M = Er/Y).[26] The crystal structure experienced evolution from the trigonal phase (phase-I) to the orthorhombic I phase (phase-II) to the orthorhombic II phase (phase-III) with the addition of Zr^{4+} (Fig. 5a). Among them, the orthorhombic II phase structure exhibited the highest ionic conductivity (σ = 1.1 × 10^{-3} S cm^{-1}), which was attributed to the tilting of the (Er/Zr)Cl_6 octahedra and the creation of additional Tet interstitial Li3 sites (Fig. 5b), strengthening the 3D Li^+ diffusion path. As shown in Fig. 5c, the ASSLB using $Li_{2.633}Er_{0.633}Zr_{0.367}Cl_6$ as the cathode electrolyte exhibited higher discharge capacity (more than 110 mAh g^{-1}) and coulombic efficiency (96.4%), superior to that of the Li_3PS_4. In fact, this phase transition process is also related to the sample preparation temperature. In another study, Park *et al.* achieved the phase transition of $Li_{3-x}Yb_{1-x}Hf_xCl_6$ from the trigonal phase to the monoclinic phase at lower annealing temperature (Fig. 5d), exhibiting higher ionic conductivity.[59] It was attributed to the fact that the presence of more Tet interstitial sites in the monoclinic phase structure played an active role in the establishment of the fast 3D diffusion network. However, as shown in Fig. 5e, the trend of ionic conductivity with doping amount is not linear. Moderate Hf^{4+} doping increases the vacancy concentration and provides more available sites for Li^+ hopping, whereas excessive Hf^{4+} doping causes a dramatic decrease in carrier concentration and contraction of lattice spacing, which in turn inhibits the Li^+ transport behavior. Therefore, designing a reasonable doping scheme to balance the vacancy content and carrier content is

Table 1 Comparisons of structure and ionic conductivity before and after chemical substitution (*T* refers to temperature)

Original materials	Crystal structures	σ (S cm^{-1})	Modified materials	Crystal structures	σ (S cm^{-1})	*T* (°C)	Ref.
Li_3ErCl_6	hcp ($P\bar{3}m1$)	8.7×10^{-5}	$Li_{2.633}Er_{0.633}Zr_{0.367}Cl_6$	hcp (*pnma* II)	1.1×10^{-3}	25	26
Li_3YCl_6	hcp (*pnma*)	6.08×10^{-5}	$Li_3Y_{0.5}In_{0.5}Cl_6$	ccp ($C2/m$)	1.51×10^{-3}	25	44
Li_3YCl_6	hcp ($P\bar{3}m1$)	1.39×10^{-4}	$Li_{2.4}Y_{0.4}Hf_{0.6}Cl_4$	hcp ($P\bar{3}m1$)	1.49×10^{-3}	RT	83
Li_3YCl_6	hcp ($P\bar{3}m1$)	—	$Li_3YBr_3Cl_3$	ccp ($C2/m$)	7.2×10^{-3}	RT	29
Li_3YbCl_6	hcp ($P\bar{3}m1$)	1.9×10^{-4}	$Li_{2.6}Yb_{0.6}Zr_{0.4}Cl_6$	ccp ($C2/m$)	1.5×10^{-3}	30	59
Li_3LuCl_6	hcp (*pnma* I)	4.0×10^{-4}	$Li_{2.5}Lu_{0.5}Zr_{0.5}Cl_6$	hcp (*pnma* II)	1.5×10^{-3}	RT	84
Li_3HoCl_6	hcp ($P\bar{3}m1$)	1.0×10^{-4}	$Li_{2.6}Ho_{0.6}Zr_{0.4}Cl_6$	hcp (*pnma* II)	1.8×10^{-3}	RT	85
Li_3HoCl_6	hcp ($P\bar{3}m1$)	1.2×10^{-4}	$Li_3HoCl_4Br_2$	ccp ($C2/m$)	1.24×10^{-3}	25	86
Li_3InCl_6	ccp ($C2/m$)	8.8×10^{-4}	$Li_{2.9}In_{0.9}Zr_{0.1}Cl_6$	ccp ($C2/m$)	1.54×10^{-3}	20	87
Li_3InCl_6	ccp ($C2/m$)	4.7×10^{-4}	$Li_{2.6}In_{0.6}Zr_{0.4}Cl_6$	ccp ($C2/m$)	1.25×10^{-3}	RT	78
Li_3InCl_6	ccp ($C2/m$)	6.7×10^{-4}	$Li_{2.7}In_{0.7}Hf_{0.3}Cl_6$	ccp ($C2/m$)	1.28×10^{-3}	25	88
Li_3InCl_6	ccp ($C2/m$)	9.7×10^{-4}	$Li_{2.6}In_{0.8}Ta_{0.2}Cl_6$	ccp ($C2/m$)	4.47×10^{-3}	30	89
Li_3InCl_6	ccp ($C2/m$)	8.49×10^{-4}	$Li_{2.75}Y_{0.16}Er_{0.16}Yb_{0.16}In_{0.25}Zr_{0.25}Cl_6$	ccp ($C2/m$)	1.17×10^{-3}	RT	90
Li_3InCl_6	ccp ($C2/m$)	9.8×10^{-4}	$Li_{2.9}In_{0.75}Zr_{0.1}Sc_{0.05}Er_{0.05}Y_{0.05}Cl_6$	ccp ($C2/m$)	2.18×10^{-3}	30	91
Li_3ScCl_6	ccp ($C2/m$)	6.7×10^{-4}	$Li_{2.5}Sc_{0.5}Zr_{0.5}Cl_6$	ccp ($C2/m$)	2.23×10^{-3}	25	92
Li_3ScCl_6	ccp ($C2/m$)	—	$Li_{2.375}Sc_{0.375}Zr_{0.625}Cl_6$	ccp ($C2/m$)	2.2×10^{-3}	25	93
$Li_2Sc_{2/3}Cl_4$	hcp (*pnma*)	1.5×10^{-3}	$Li_2Sc_{0.222}In_{0.444}Cl_6$	hcp ($Fd\bar{3}m$)	2.0×10^{-3}	25	30
Li_2ZrCl_6	hcp ($P\bar{3}m1$)	4.0×10^{-4}	$Li_{2.25}Zr_{0.75}Fe_{0.25}Cl_6$	hcp ($P\bar{3}m1$)	9.8×10^{-4}	30	43
Li_2ZrCl_6	ccp ($C2/m$)	7.1×10^{-6}	$Li_{2.7}Zr_{0.3}(In/Sc)_{0.7}Cl_6$	ccp ($C2/m$)	2.1×10^{-3}	30	94
Li_2ZrCl_6	hcp ($P\bar{3}m1$)	5.7×10^{-6}	$Li_{2.5}Zr_{0.5}Y_{0.5}Cl_6$	hcp ($P\bar{3}m1$)	1.19×10^{-3}	RT	95
Li_2ZrCl_6	hcp ($P\bar{3}m1$)	1.2×10^{-4}	$Li_{2.25}Zr_{0.75}Al_{0.25}Cl_6$	hcp ($P\bar{3}m1$)	1.13×10^{-3}	25	96
Li_2ZrCl_6	hcp ($P\bar{3}m1$)	3.0×10^{-4}	$Li_{2.1}Zr_{0.95}Mg_{0.05}Cl_6$	hcp ($P\bar{3}m1$)	6.2×10^{-4}	25	97
Li_2ZrCl_6	hcp ($P\bar{3}m1$)	4.0×10^{-4}	$Li_{2.1}Zr_{0.95}Mn_{0.05}Cl_6$	hcp ($P\bar{3}m1$)	8.0×10^{-4}	RT	98
Li_2ZrCl_6	hcp ($P\bar{3}m1$)	3.3×10^{-4}	$Li_{3.1}ZrCl_{4.9}O_{1.1}$	ccp ($C2/m$)	1.3×10^{-3}	25	99
Li_2ZrCl_6	hcp ($P\bar{3}m1$)	3.97×10^{-4}	$Li_{3.4}ZrCl_{4.6}O_{1.4}$	ccp ($C2/m$)	1.46×10^{-3}	25	100
Li_2ZrF_6	hcp ($P\bar{3}m1$)	—	Li_2ZrF_5Cl	hcp ($P\bar{3}m1$)	5.5×10^{-7}	25	101
Li_2HfCl_6	hcp ($P\bar{3}m1$)	3.98×10^{-4}	$Li_{2.3}Hf_{0.7}In_{0.3}Cl_6$	ccp ($C2/m$)	1.05×10^{-3}	30	102

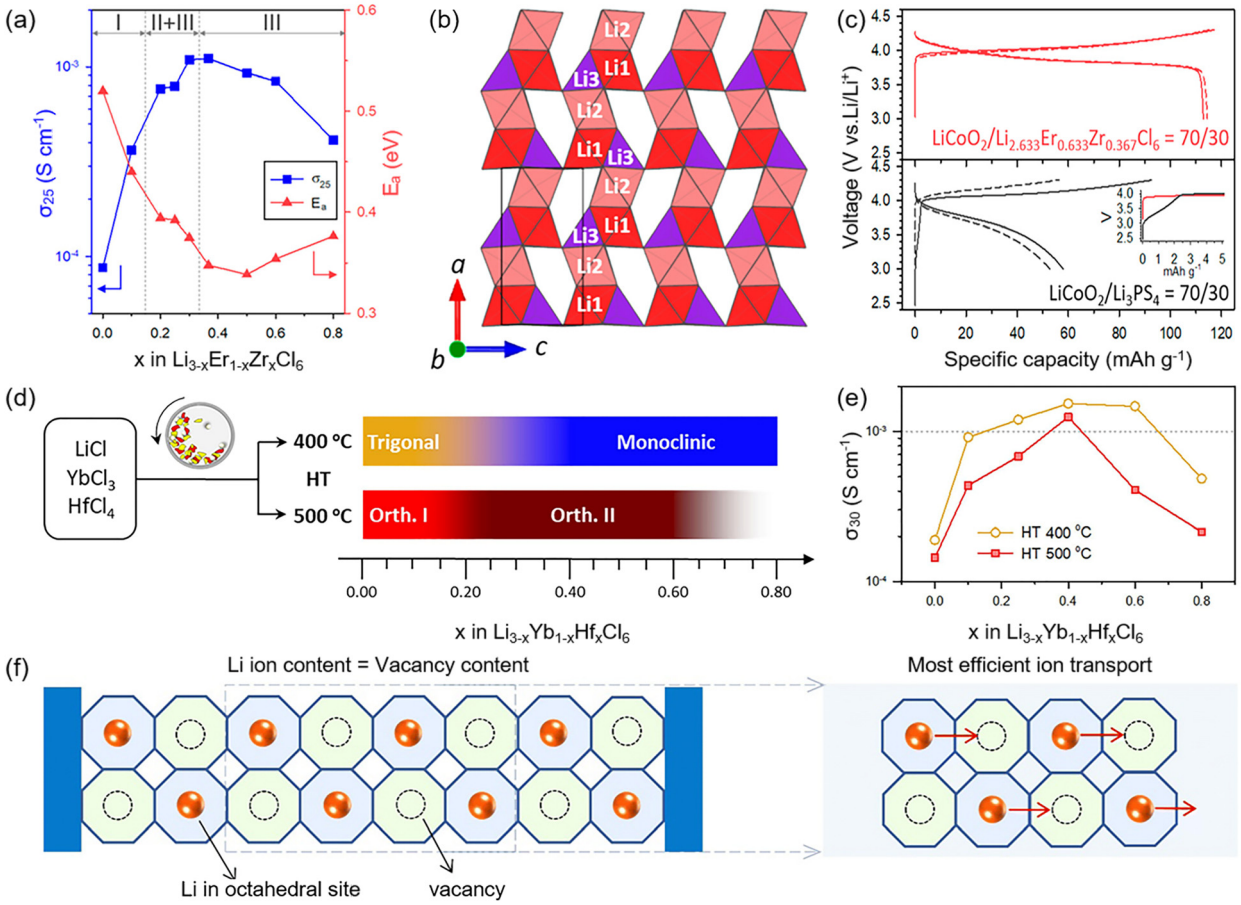

Fig. 5 Effect of aliovalent substitution on halide phase evolution and ionic conductivity. (a) Phase evolution and corresponding ionic conductivities for $Li_{3-x}Er_{1-x}Zr_xCl_6$. (b) Li^+ connection along the (100) direction. (c) Charge–discharge voltage profiles of ASSLBs using different SSEs. Reproduced with permissions from ref. 26. Copyright 2020, American Chemical Society. (d) Phase evolution of $Li_{3-x}Yb_{1-x}Hf_xCl_6$ annealed at different temperatures. (e) Changes in ionic conductivity at different temperatures for $Li_{3-x}Yb_{1-x}Hf_xCl_6$. Reproduced with permissions from ref. 59. Copyright 2021, Elsevier. (f) Effect of the correlation between vacancy concentration and Li-ion content on ion transport. Reproduced with permissions from ref. 84. Copyright 2023, The Royal Society of Chemistry.

the key to modulating ion transport behavior. This is evidenced in the study of Wang *et al.*, who concluded that the optimal ion transport behavior can only be realized when the vacancy concentration is equal to the carrier concentration (Fig. 5f).[84]

It is worth mentioning that not all aliovalent substitutions cause the transformation of intrinsic structure such as $Li_{3-x}In_{1-x}(Zr/Hf)_xCl_6$ and $Li_{3-x}Sc_{1-x}(Zr/Hf)_xCl_6$, which maintain the ccp structure throughout the solid solution range.[87,88,105,106] Because their ionic radii are very similar, doping does not make the average ionic radius of the central metal change significantly. For these compounds, aliovalent substitution enhances ionic conductivity mainly by the synergistic effect of the Li^+ sublattice rearrangement and migration path optimization. In the case of Li_3InCl_6 with a typical layered structure (Fig. 6a), In^{3+} is only distributed in the (001) plane, while Li^+ occupies both the (001) and (002) plane.[78] After doping Zr^{4+}, the Li^+ on the Tet interstitial site Li3 disappears, and the Li^+ content on the M2/Li4 site increases, implying that Li^+ is more preferred in occupying the M2/Li4 site with the mixed cation distribution. The former provides more vacancies for Li^+ migration along the *ab*-plane, the latter raises Li^+ diffusion rate along the *c*-axis due to the weakened coulombic repulsion from high-valence cations. The redistribution of Li^+ sites leads to the formation of migration channels (Li1/Li2–Li3–M2/Li4–Li3–Li1/Li2) with lower activation barriers (Fig. 6b), enhancing the 3D Li^+ diffusion. Similarly, the enhanced 3D diffusivity can also be explained by the change in the preferred orientation of lattice plane.[87] For example, by doping Zr^{4+} in Li_3ScCl_6, Li *et al.* made the original random orientation *ab* planes tend to be aligned in a uniform orientation (Fig. 6c), which reduced the migration resistance of Li^+ conduction in all directions (Fig. 6d), especially in the *ab* plane.[92] This optimized ion migration behavior was also reflected by the excellent rate capability of the battery (Fig. 6e). Notably, it is not difficult to find in Fig. 6d that the Li^+ conduction along the *c*-axis was the speed control step, which determined the overall Li^+ migration rate. Therefore, the effect of

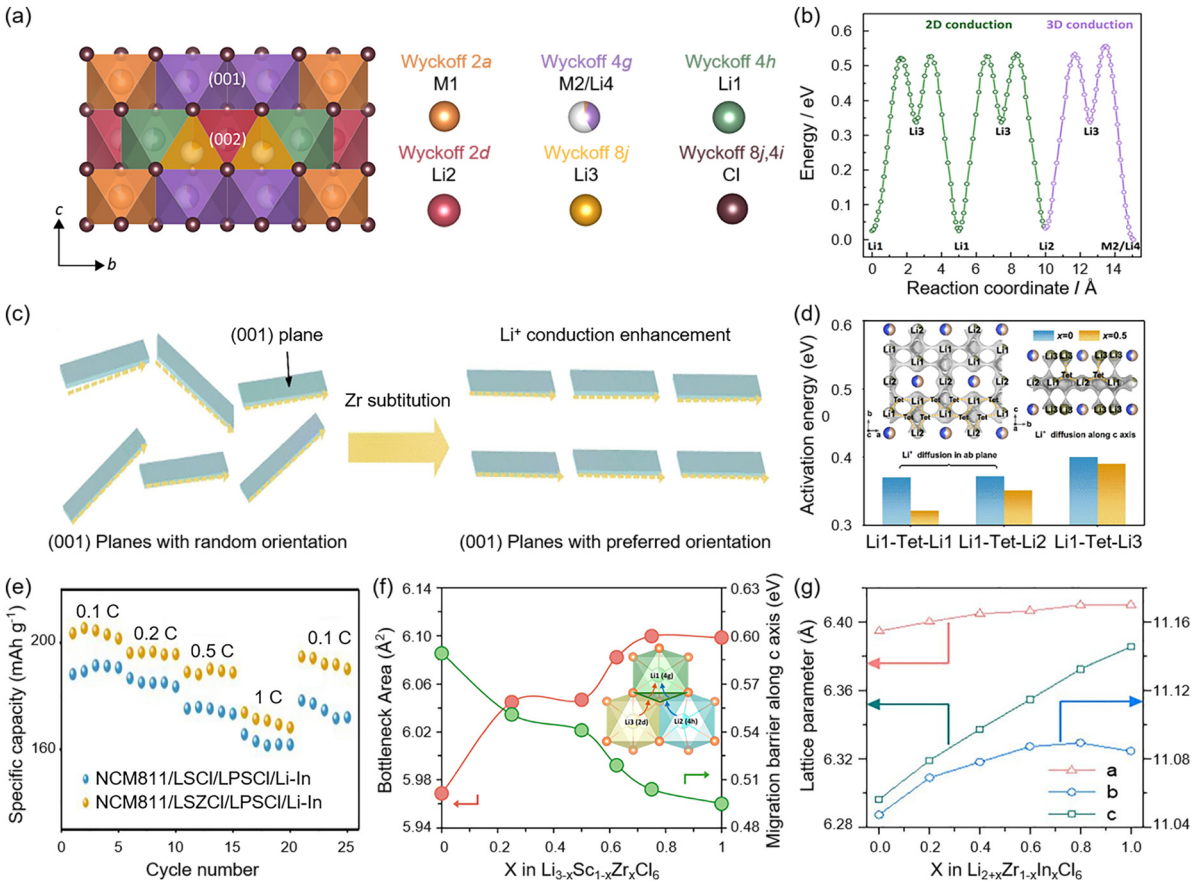

Fig. 6 Cation site distribution and migration pathway affected by aliovalent substitution. (a) Crystal structure of Li_3InCl_6. (b) Optimal Li^+ diffusion pathway from bond valence sum calculations. Reproduced with permissions from ref. 78. Copyright 2021, American Chemical Society. (c) Schematic illustration of Zr^{4+} substitution changing the (001) plane preferred orientation. (d) Comparison of activation energy through different migration pathways before and after Zr^{4+} doping. (e) Rate capability of batteries after Zr^{4+} doping. Reproduced with permissions from ref. 92. Copyright 2022, Elsevier. (f) Change in the bottleneck area and migration barrier for Li^+ diffusion along the *c*-axis. The inset depicts the bottleneck area for Li^+ migration along the *c*-axis. Reproduced with permissions from ref. 93. Copyright 2024, American Chemical Society. (g) Correlation curves of lattice parameter with In^{3+} doping amount. Reproduced with permissions from ref. 94. Copyright 2022, Elsevier.

Zr^{4+} substitution on the change of *c*-axis channel size in Li_3ScCl_6 was carefully considered. The researchers found that the triangular bottleneck area for Li^+ migration along the *c*-axis was increased with the increase of Zr^{4+} (Fig. 6f), which lowered the migration barrier of the *c*-axis, obtaining a higher ionic conductivity.[93]

Recently, Li_2ZrCl_6 has attracted much attention due to its cost-effectiveness and good environmental stability, but the lower ionic conductivity restricts its further development, and is related to its insufficient number of carriers.[107–109] In view of this, Kwak and his coworkers doped In^{3+}/Sc^{3+} in Li_2ZrCl_6 to increase the carrier content in the (002) plane, favoring the more convenient Li^+ migration along the *ab* plane.[94] At the same time, due to the difference in electronegativity of the central metal elements, mixed ionic-covalent bonding is formed in the crystal structure and local anisotropic lattice expansion is triggered (Fig. 6g). The existence of mixed ion–covalent bonding is the signature characteristic of rapid Li^+ transport. In addition, attempts to dope trivalent low-cost metal elements (such as Fe^{3+}, Al^{3+}) and divalent metal elements (such as Mg^{2+}, Mn^{2+}) into Li_2ZrCl_6 have also been shown to effectively improve ionic conductivity by increasing carrier contents and broadening migration channels.[43,96–98]

3.2 Isovalent cation substitution

Compared with aliovalent substitution, the isovalent substitution of the central metal cation does not affect the carrier content and vacancy content. Instead, it enhances the ionic conductivity mainly by changing the basic structural framework or migration channel size due to the difference in ionic radii. Li *et al.* elevated the ionic conductivity of Li_3YCl_6 by doping In^{3+}, and its structure was gradually converted from hcp structure to ccp monoclinic phase structure (Fig. 7a).[44] In particular, the ionic conductivity of all samples reached 1×10^{-3} S cm^{-1} when the doping amount exceeded 50%, which confirms that the monoclinic phase structure is the most favorable structure for Li^+ conduction. It is worth mentioning that In^{3+} doping also significantly improves the humidity stability of $Li_3Y_{1-x}In_xCl_6$, which is attributed to the formation of $Li_3Y_{1-x}In_xCl_6{\cdot}xH_2O$ intermediates to prevent the hydrolysis of

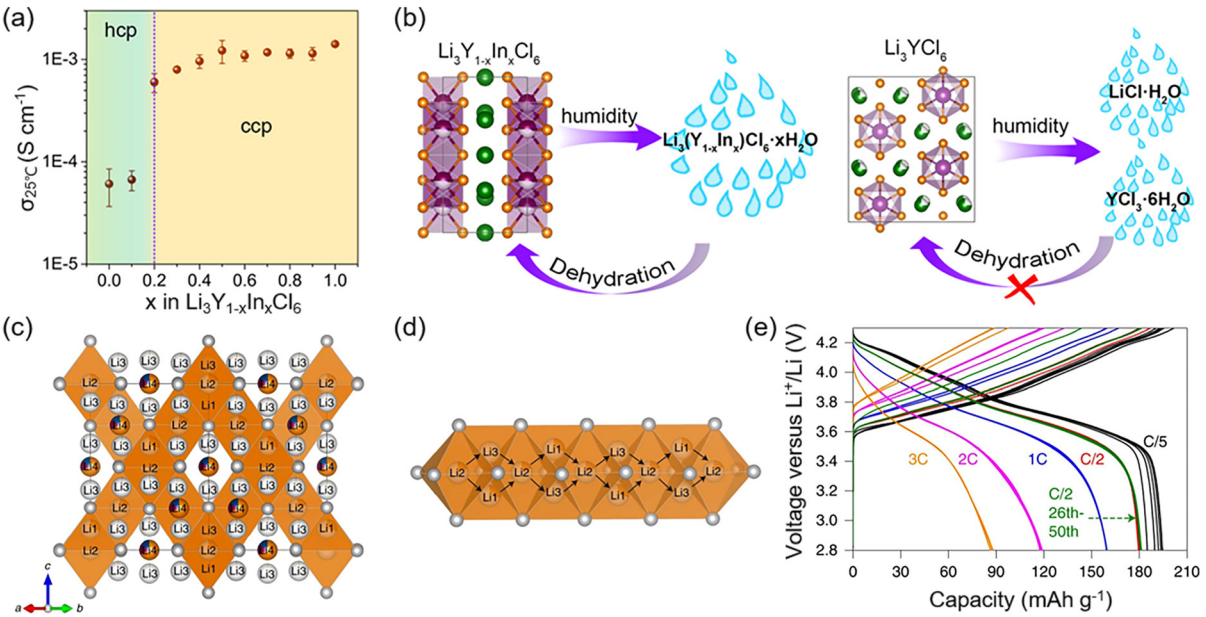

Fig. 7 Influence of isovalent substitution of central metal cation on chemical/electrochemical stability. (a) Li^+ conductivity at 25 °C for $Li_3Y_{1-x}In_xCl_6$ and corresponding phase transitions. (b) Comparison of humidity stability between $Li_3Y_{1-x}In_xCl_6$ and Li_3YCl_6. Reproduced with permissions from ref. 44. Copyright 2020, American Chemical Society. (c) The main 3D Li^+ diffusion channels of $Li_2Sc_{0.666-x}In_xCl_6$. (d) Enlarged pathways of Li^+ diffusion between tetrahedra and octahedra. (e) Charge–discharge curves of the ASSLB loaded with $Li_2In_{1/3}Sc_{1/3}Cl_6$ at different rates. Reproduced with permissions from ref. 30. Copyright 2022, Springer Nature.

Li_3YCl_6 (Fig. 7b). Inspired by $Li_3Y_{1-x}In_xCl_6$, Zhou *et al.* synthesized the chlorospinels $Li_2Sc_{0.666-x}In_xCl_6$ ($0 \le x \le 0.666$), which exhibited high ionic conductivity ($1.83–2.03 \times 10^{-3}$ S cm^{-1}) over the entire compositional range.[30] It was associated with the low occupancy of Oct sites and Tet interstitial sites, providing more vacancy sites and forming the 3D Li^+ diffusion channel with a lower migration barrier (Fig. 7c and d). Particularly, the ASSLB assembled with $Li_2In_{1/3}Sc_{1/3}Cl_6$ also displayed favorable charge–discharge behavior and rate capability when matched with $LiNi_{0.85}Co_{0.1}Mn_{0.05}O_2$ (NCM85), as shown in Fig. 7e. In addition, although some computational simulations have shown that La^{3+} has the potential to enhance ionic conductivity by increasing the lattice size and broadening the migration channels due to the larger ionic radius, further experiments are needed for validation.[110,111]

3.3 Anion substitution

As the skeleton ions constituting the bulk structure of halide SSEs, the local coordination environment of halogen ions plays a crucial role in the ion transport rate. By changing the polarization of the Li–X bond, modifications in the lattice parameters and even anion sublattice stacking style can be triggered.

Based on the fact that the more polarizable anion sublattice is more beneficial for Li^+ migration, Tomita and his group explored the effect of different halogen doping on the crystal structure and ionic conductivity in Li_3InBr_6.[21,112] As expected, F^- doping caused the contraction of the lattice parameter and the decrease in ionic conductivity, while I^- doping led to the expansion of the lattice parameter and the increase in ionic conductivity. Surprisingly, because Cl^- doping is ordered enough to compensate for the negative effects of lattice shrinkage, the ionic conductivity was also ultimately improved. The substitution mechanism was further explained in studies regarding $Li_3HoCl_{6-x}Br_x$, $Li_3HoBr_{6-x}I_x$ and $Li_2ZrF_{6-x}Cl_x$.[80,86,101] For example, Plass *et al.* obtained faster Li^+ diffusion channels with low migration barriers by doping Li_3HoBr_6 with I^-, which has a larger ionic radius and lower electronegativity. This effect originated from the increase in interplanar distance and coordination polyhedral volume, which led to the widening of Li^+ diffusion channels. Meanwhile, the weaker bond strength between Li^+ and X^- led to the weakening of the binding force of the skeleton ion against Li^+. It should be noted that the doping amount of I^- should not be excessive, as this affects the mixed distribution of cation sites in the lattice and increases the electrostatic repulsion, thus inhibiting the rapid Li^+ diffusion and lowering the ionic conductivity.

Besides lattice expansion and lattice softening, anion substitution can also induce a change in the anion sublattice stacking style. Liu *et al.* prepared a new halide family $Li_3MBr_3Cl_3$ (M = Y/Er), by mechanochemical milling and hot-pressing (HP) treatment, which exhibited the same ccp monoclinic phase structure as the endmember Li_3YBr_6.[29] $Li_3YBr_3Cl_3$ achieved ultrahigh ionic conductivity (~7.2×10^{-3} S cm^{-1}), which was the result of synergistic modulation of the two factors. On the one hand, due to the mixed distribution of Li^+ in the Oct and Tet interstitial sites, more vacancies were gener-

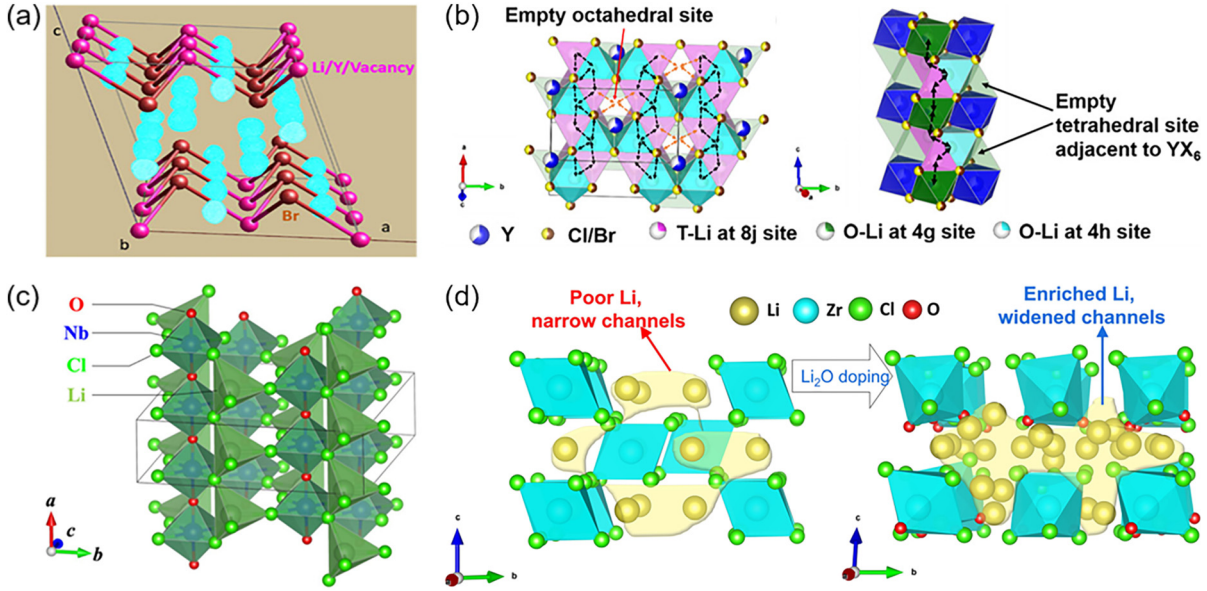

Fig. 8 Modification of crystal structure and Li^+ site distribution by anion substitution. (a) Mixed Tet–Oct distribution of Li^+ revealed *via* Fourier difference map from neutron diffraction of LYBC-HP. (b) Optimized Li^+ 3D diffusion pathway due to increased vacancy content at Oct sites. Reproduced with permissions from ref. 29. Copyright 2020, American Chemical Society. (c) Crystal structure of $LiNbOCl_4$. Reproduced with permissions from ref. 114. Copyright 2023, Wiley-VCH. (d) Effect of O^{2-} doping on carrier concentration and migration channels. Reproduced with permissions from ref. 100. Copyright 2024, Elsevier.

ated in the Oct site and the energy barrier was lowered (Fig. 8a and b), thus optimizing the 3D Li^+ diffusion channel. On the other hand, the hot-pressing-treated samples formed denser blocks and better grain boundary contacts, which greatly reduced the grain boundary impedance and benefited the overall ionic conductivity. The high conductivity of $Li_3YBr_3Cl_3$ was further explained by a first-principles study.[113] Intralayer vacancy diffusion in the Li layer promotes interlayer concerted diffusion between different metal layers, which accelerates the Li^+ transport rate.

Significantly, although it is widely believed that O^{2-} with high electronegativity is not favorable for fast ionic conduction, many recent studies have demonstrated that O^{2-} doping possesses unique advantages in enhancing ionic conductivity.[115,116] As shown in Fig. 8c, Tanaka *et al.* reported a new oxyhalide SSE, $LiMOCl_4$ (M = Nb/Ta), belonging to the orthorhombic structure (space group: *Cmc*21), in which O^{2-} is only responsible for connecting the octahedra together.[114] The addition of O^{2-} broadened the bottleneck size of the Li^+ diffusion channel (1.939 Å), achieving an ultrahigh ionic conductivity of 1.07×10^{-2} S cm^{-1}, which is comparable to those of liquid electrolytes. In addition, O^{2-} doping can also affect the ionic conductivity by changing the crystal structure and Li^+ site distribution. Park and Cheng *et al.* achieved a structural transition from the hcp trigonal phase to the ccp monoclinic phase by increasing the amount of O^{2-} doping in Li_2ZrCl_6.[99,100] Accompanied by the stabilization of Li interstitial sites and the enrichment of carrier concentration (Fig. 8d), the ion transport channel was broadened and the ionic conductivity was successfully raised above 1×10^{-3} S cm^{-1}. Interestingly, O^{2-} doping seems to enhance the amorphous proportion of halide SSEs, which is extremely important for inducing polyhedrons distortions and lowering the migration barriers.[34,117,118] Similar amorphous characteristics have been observed in recent studies on nitrogen doping. The $Li_{3x}TaCl_5N_x$ synthesized by Hong *et al.* exhibits a highly amorphous structure, demonstrating exceptional ionic conductivity (up to 7.34×10^{-3} S cm^{-1}), significantly exceeding that of most conventional halide SSEs.[35] This remarkable performance was attributed to the incorporation of nitrogen, which alters the local coordination environments of both cations and anions, thereby establishing a unique and efficient Li^+ migration mechanism within the amorphous structure.

3.4 Double-doping strategy

In order to provide halide SSEs with both high conductivity and excellent interfacial stability, double-doping strategies have emerged as a concern. For example, Subramanian *et al.* prepared $Li_{2.4}Y_{0.4}Zr_{0.6}Cl_{5.85}F_{0.15}$ SSE through the high-energy ball milling method.[119] Among them, Zr^{4+} doping increased the vacancy concentration and cation disorder, and a high ionic conductivity of 1.45×10^{-3} S cm^{-1} was obtained, whereas F^- doping contributed to the formation of stable Li^+-conducting cathode–electrolyte interphase (CEI), and the electrochemical window was widened to 1.29–3.9 V. In addition, structural modulation by the double-doping strategy was also observed in a UCl_3-type $LaCl_3$ SSE. Hao *et al.* achieved high ionic conductivity and superior compatibility with Li metal by doping both Zr^{4+} and O^{2-} in a $LaCl_3$-based SSE.[64] It was attributed to the Zr^{4+}–O^{2-} co-doping strategy that makes the anion

sublattice more stable and smoothes the 1D Li^+ transport channel. Indeed, such a double-doping strategy can be further extended to multi-ion doping.[91,120] Song and his group synthesized the high-entropy halide SSE $Li_{2.75}Y_{0.16}Er_{0.16}Yb_{0.16}In_{0.25}Zr_{0.25}Cl_6$ (HE-LIC) by replacing In^{3+} in LIC with various metal elements.[90] The local lattice distortion triggered by the high entropy effect effectively improved the diffusion kinetics of Li^+ and Cl^-, which enhanced the Li^+ conductivity and oxidation stability.

In summary, the chemical substitution of halide SSEs can tune the vacancy concentration and modify the Li^+ migration channel, thereby attaining aliostructural/isostructural alloy halides with higher ionic conductivity. Nevertheless, more efforts are expected to explore the feasibility of multi-element doping in order to further enrich the halide SSEs family to improve its competitiveness in the SSEs field.

4. Interface modification by chemical substitution

In addition to the ionic conductivity of SSEs, interfacial issues between SSEs/electrodes should not be neglected, as they significantly affect the coulombic efficiency, rate capability and cycle life of ASSLBs.[45,121–124] In order to construct high-energy and long-life ASSLBs, it is necessary to investigate the electrochemical stability of halide SSEs and effectively regulate the interface behavior through modification strategies.

4.1 Intrinsic electrochemical stability

The electrochemical stability of SSEs is closely related to the electrochemical stability window, the upper and lower limits of which represent the plating/stripping potentials, respectively, in which SSEs do not suffer from any redox reactions. And SSE with a wide electrochemical stability window can be better matched with high-voltage cathode active materials and high specific capacity Li metal anode to maximize the energy density of ASSLBs and achieve stable cycling. As shown in Fig. 9a, Mo *et al.* evaluated the thermodynamic equilibrium voltage curves and phase equilibria of Li_3YCl_6 and Li_3YBr_6 by theoretical calculations, both of which have a wide electrochemical window (Li_3YCl_6: 0.62–4.21 V; Li_3YBr_6: 0.59–3.15 V), hoping to achieve great contact with the electrodes.[66] The relationship between the thermodynamic intrinsic electrochemical window and composition of halide SSEs is specified in Fig. 9b, where the F^- and Cl^--based halides indeed exhibit high oxidation potentials. However, the calculation results of the mutual energy between chloride SSEs and cathode materials show that chloride SSEs exhibit high mutual energy (~100 meV) when matched with the high-pressure ternary system NCM (Fig. 9c).[125] It is well above the threshold for the interfacial reaction to occur, implying that the severe interfacial reaction is occurring. As for the reduction stability at low potentials, even though the group III elements represented by the Sc, Y, and La–Lu exhibit the lowest reduction potentials (0.41–0.92 V *vs.* Li^+/Li), it is still higher relative to the Li metal anode.[66]

In order to improve the high-voltage stability and reduction stability of halide SSEs, current modification measures include adding a coating or buffer layer between the electrode materials and SSEs.[27,126–129] However, this increases the assembly cost of ASSLBs and is not suitable for commercial production. Chemical substitution can affect the degree of electron localization between M and X due to the difference in electronegativity, thus determining the oxidation and reduction potentials. Tham *et al.* explored the influence of different substitution types on the electrochemical stability of halide SSEs with the help of first-principles calculations.[130] They suggested that doping halogen ions with higher electronegativity yields higher oxidation potentials, while doping cations with lower electronegativity obtains lower reduction potentials due to the weakened attraction against electrons. This provides design guidelines for the experimental synthesis of halide SSEs with excellent electrochemical stability. Furthermore, the volume change at the SSEs/electrode interface is also crucial for interfacial compatibility; in particular, the Ni-based cathode material has serious volume shrinkage under high pressure, resulting in cracks and contact loss at the interface, which decays the cycle performance.[131–133] The partially substituted halides shown in Fig. 9d demonstrate excellent mechanical stability and are expected to be key components in high-voltage batteries.[130] The battery configurations and electrochemical performances of ASSLBs using halide SSEs are summarized in Table 2.

4.2 Stability of halide SSEs towards Li metal anode

In view of the poor reduction stability of halide SSEs, when they are directly matched with Li metal anode, continuous interfacial reaction and lithium puncture will occur, shortening battery life and even causing safety problems. For example, the contact of Li_3MCl_6 with the Li metal anode leads to the occurrence of a reduction reaction, in which M^{3+} is reduced to M^0.[134,135] M^0 and another reaction product, LiCl, form a mixed ion–electron conduction (MIEC) interface (Fig. 10a), where successive electrons pass through the interface to drive the continuation of the thermodynamically favorable reduction reaction. The continued accumulation of reaction products rapidly increases the interfacial impedance and eventually gives rise to battery failure as Li_3MCl_6 or Li metal is depleted. This was confirmed by Riegger *et al.* in their study on the interfacial compatibility between Li_3InCl_6 and Li metal anode.[135] As shown in Fig. 10b, the interfacial impedance increased with time, which was attributed to the non-self-limiting interfacial reaction between the Li_3InCl_6 and the Li metal anode.

In liquid batteries, LiF is the key component for stabilizing SEI membranes due to its wide electrochemical window, excellent ionic conductivity and electronic insulation as well as suitable elastic modulus.[140–142] Correspondingly, constructing an *in situ*-formed F-rich interfacial layer at the SSEs/Li metal anode interface can effectively inhibit the formation of the MIEC interface and lithium dendrite growth (Fig. 10a).[143–145]

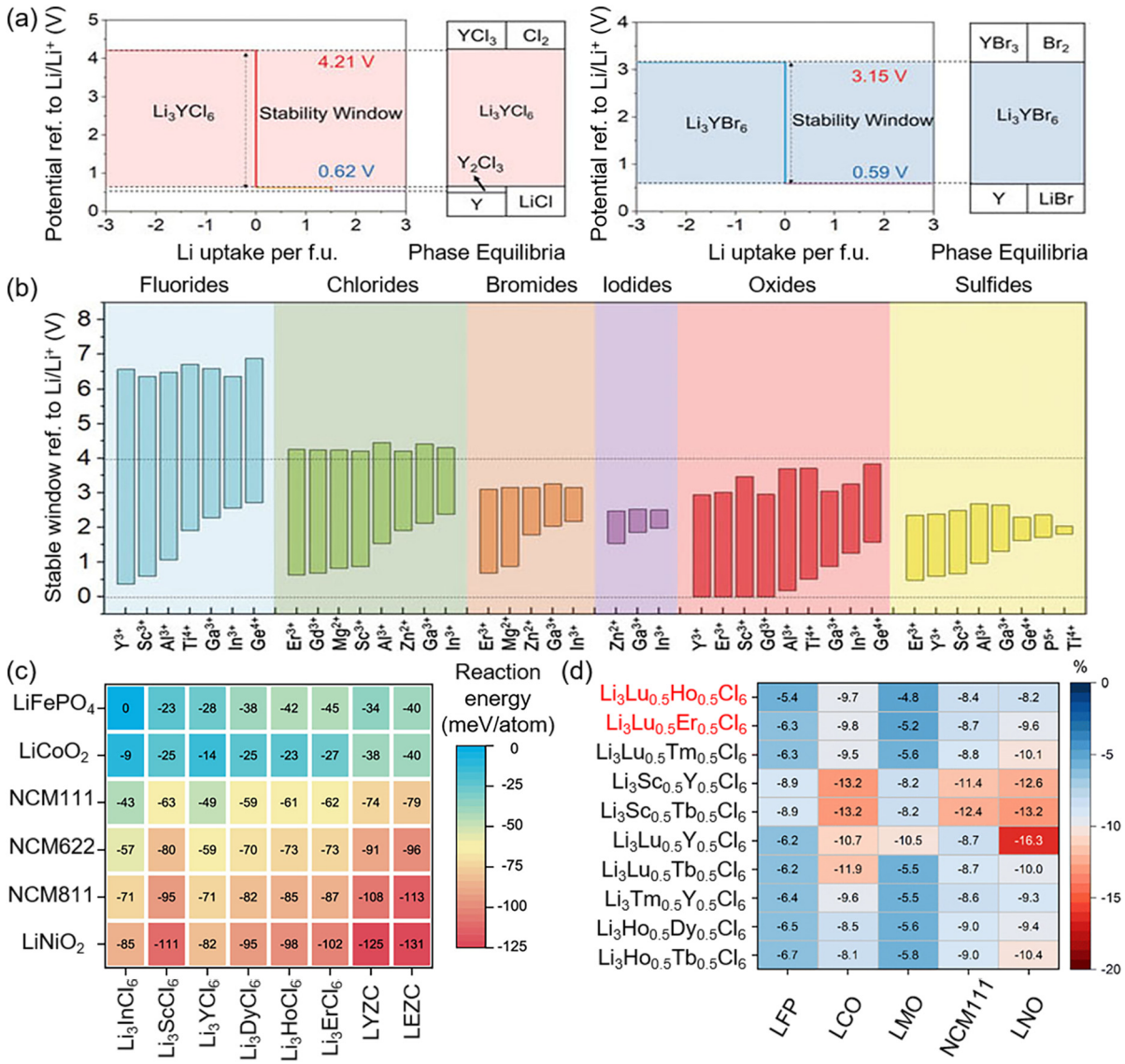

Fig. 9 Intrinsic electrochemical stability of halide SSEs. (a) The thermodynamic equilibrium voltage profile and phase equilibria for Li_3YCl_6 and Li_3YBr_6. (b) Calculated thermodynamics of inherent electrochemical windows for Li–M–X ternary compounds (M = cation, X = F, Cl, Br, I, O, S). Reproduced with permissions from ref. 66. Copyright 2019, Wiley-VCH. (c) Mutual reaction energy between common cathodes and halide SSEs. Reproduced with permissions from ref. 125. Copyright 2021, American Chemical Society. (d) The percentage volume changes caused by the SSEs/cathode interfacial reaction. Compounds are mechanically stable with a percent change in volume of less than 10%. Reproduced with permissions from ref. 130. Copyright 2023, The Royal Society of Chemistry.

Yu *et al.* attempted to dope F^- into Li_3YBr_6 to improve the degradation of Li_3YBr_6 in contact with the Li metal anode.[136] The assembled Li//$Li_3YBr_{5.7}F_{0.3}$//LCO@LIC battery maintained a higher discharge capacity even after 70 cycles (Fig. 10c), which was attributed to the findings from the investigation of the SSE/Li interface post-cycling. XPS depth profiling results revealed that the characteristic peak of the Li–F bond at ≈684.7 eV gradually increased with increasing etching level, indicating the formation of abundant LiF at the interface (Fig. 10d). This was corroborated by the SEM image of the SSE/Li interface, which showed a dense and homogeneous F-rich interfacial layer with a reticular structure (Fig. 10e). The *in situ* F-rich interfacial layer not only passivated side reactions at the interface but also mitigated the excessive stress caused by inhomogeneous Li deposition, thereby inhibiting the growth of lithium dendrites.

Interestingly, the amorphous content of the material also seems to influence the reduction potential. For example, the reduction potential of amorphous and crystalline $Li_{0.35}La_{0.55}TiO_3$ differs by 0.5 V.[146] Hu *et al.* obtained materials with more amorphous content by doping O^{2-} in Li_2ZrCl_6; as a result $Li_{1.75}ZrCl_{4.75}O_{0.5}$ exhibited a reduction potential of 0.37 V lower than that of Li_2ZrCl_6.[116] However, the magnitude of this reduction was not sufficient to achieve direct compatibility

Table 2 Summary of battery design and electrochemical performances of ASSLBs using halide SSEs (LCO: $LiCoO_2$; NCM811: $LiNi_{0.8}Co_{0.1}Mn_{0.1}O_2$; NCM622: $LiNi_{0.6}Co_{0.2}Mn_{0.2}O_2$; NCM85: $LiNi_{0.85}Co_{0.1}Mn_{0.05}O_2$; NCM955: $LiNi_{0.90}Co_{0.05}Mn_{0.05}O_2$; NCM523: $LiNi_{0.5}Co_{0.2}Mn_{0.3}O_2$)

			Electrochemical performances (mA h g^{-1})		
Battery configurations	T (°C)	Voltage range (V *vs.* Li^+/Li)	Current density/specific capacity/initial coulombic efficiency (ICE)	Current density/cycle number/specific capacity/capacity retention	Ref.
Li–In//Li_3YCl_6//LCO	25	2.5–4.2	0.44C/~117/94.8%	0.1C/100/~114/98%	22
$Li_{11}Sn_6$//Li_3PS_4//LCO@$Li_{2.633}Er_{0.633}Zr_{0.367}Cl_6$	RT	3–4.3	0.1C/~112/96.4%	0.5C/200/~80/—	26
Li–In//Li_6PS_5Cl//$Li_{2.4}Y_{0.4}Hf_{0.6}Cl_6$//LCO	RT	2.9–4.2	0.1C/120/93%	0.1C/100/~80/70%	83
Li//$Li_{5.3}PS_{4.3}Cl_{1.0}Br_{0.7}$//$Li_{2.4}Y_{0.6}Zr_{0.4}Cl_{5.85}F_{0.15}$/ /NCM811	RT	2.5–4.25	0.1C/190/87%	0.5C/250/128/95.5%	119
Li//Li_3YBr_6//LCO@LIC	RT	2.5–4.2	0.14 mA cm^{-2}/126.7/89%	0.14 mA cm^{-2}/70/~15/12%	136
Li//$Li_3YBr_{5.7}F_{0.3}$//LCO@LIC	RT	2.5–4.2	0.14 mA cm^{-2}/121.6/90%	0.14 mA cm^{-2}/70/~73/60%	136
Li–In//$Li_{6.7}Si_{0.7}Sb_{0.3}S_5I$//$Li_{2.7}Yb_{0.7}Zr_{0.3}Cl_6$//NCM622	RT	2.8–4.3	0.2C/170/—	0.2C/150/136/80%	103
Li–In//$Li_{10}GeP_2S_{12}$//$Li_{2.556}Yb_{0.492}Zr_{0.492}Cl_6$//LCO	25	2.5–4.5	0.1C/193.9/93.3%	0.3C/50/149.7/82.1%	60
In//$Li_{10}GeP_2S_{12}$//Li_3InCl_6//NCM811	25	2.5–4.4	0.13 mA cm^{-2}/154/84.2%	0.13 mA cm^{-2}/70/150/97.4%	23
Li–In//Li_6PS_5Cl//Li_3InCl_6//LCO	RT	3–4.2	0.1C/104.4/92.2%	0.1C/50/~57/54.5%	88
Li–In//Li_6PS_5Cl//$Li_{2.7}In_{0.7}Hf_{0.3}Cl_6$//LCO	RT	3–4.2	0.1C/108.1/96.8%	0.1C/50/~7871.7%	88
Li–In//Li_6PS_5Cl//$Li_{2.6}In_{0.8}Ta_{0.2}Cl_6$//LCO	30	3–4.6	4C/~135/—	4C/1400/~95/70%	89
In//Li_6PS_5Cl//Li_3InCl_6//LCO@$Li_3InCl_{4.8}F_{1.2}$	RT	2.6–4.47	0.063 mA cm^{-2}/160.6/92%	0.125 mA cm^{-2}/70/102/—	28
In//Li_3ScCl_6//LCO	25	2.5–4.2	0.13 mA cm^{-2}/126.2/90.3%	0.13 mA cm^{-2}/160/104.5/82.8%	39
Li–In//Li_6PS_5Cl//$Li_{2.5}Sc_{0.5}Zr_{0.5}Cl_6$//NCM811	RT	2.8–4.3	0.1C/203.6/89.6%	0.2C/200/174.5/90%	92
Li–In//$Li_{6.7}Si_{0.7}Sb_{0.3}S_5I$//$Li_2Sc_{2/3}Cl_4$//NCM622	RT	2.8–4.3	0.5C/~170/—	0.1C/110/170/—	41
Li–In//$Li_{6.7}Si_{0.7}Sb_{0.3}S_5I$//$Li_2Sc_{1/3}In_{1/3}Cl_4$//NCM85	RT	2.8–4.8	0.2C/~215/—	0.2C/110/~205/95%	30
Li–In//Li_6PS_5Cl//Li_2ZrCl_6//LCO	25	2.5–4.2	14 mA g^{-1}/137/97.9%	70 mA g^{-1}/100/114/—	107
Li–In//Li_6PS_5Cl//Li_2ZrCl_6//NCM811	25	2.98–4.18	0.1C/152.3/84.3%	0.1C/100/~133/87.4%	96
Li–In//Li_6PS_5Cl//$Li_{2.25}Zr_{0.75}Al_{0.25}Cl_6$//NCM811	25	2.98–4.18	0.1C/166.8/87.2%	0.1C/100/~157/94.3%	96
Li–In//Li_6PS_5Cl//$Li_{2.8}Zr_{0.2}In_{0.8}Cl_6$//NCM811	25	2.82–4.42	0.2C/174.5/87.5%	1C/500/~110/74%	137
Li–In//Li_6PS_5Cl//$Li_{2.1}Zr_{0.95}Mg_{0.05}Cl_6$//LCO	25	3–4.3	0.1C/147/96.6%	0.3C/100/121.3/~87.1%	97
Li–In//$LZCl_{5.6}F_{0.4}$//LCO	30	2.52–4.32	0.1C/132/95.57%	0.5C/70/86.4/76%	138
Li–In//Li_6PS_5Cl//$Li_{1.75}ZrCl_{4.75}O_{0.5}$//LCO	25	2.48–4.18	14 mA g^{-1}/137.5/98.28%	700 mA g^{-1}/150/102/—	116
Li–In//Li_6PS_5Cl//$Li_{2.5}ZrCl_5F_{0.5}O_{0.5}$//NCM955	RT	2.5–4.35	0.1C/207.1/—	0.5C/500/125.8/81.2%	139
Li//$Li_{0.388}Ta_{0.238}La_{0.475}Cl_3$//NCM523	30	2.20–4.35	0.44C/163/84.96%	0.44C/100/~133.8/81.6%	32
Li–In//Li_3YCl_6//$Li_{1.25}TaCl_5N_{0.42}$//NCM811	25	3–4.3	0.5C/~130/—	0.5C/350/124.4/95.47%	35
Li–In//Li_6PS_5Cl//LiAlOCl-981//LCO	25	2.5–4.3	0.1C/145.85/97.3%	0.5C/300/~117/86.95%	118
Li–In//Li_6PS_5Cl//HE-LIC//LCO	25	2.5–4.2	0.1C/144/97%	0.5C/500/~115/88.9%	90

between $Li_{1.75}ZrCl_{4.75}O_{0.5}$ and the bare Li metal anode, as demonstrated by the high overpotential (~0.7 V) observed during cycling of the assembled Li//$Li_{1.75}ZrCl_{4.75}O_{0.5}$//Li symmetric battery. Therefore, the incorporation of an intermediate layer, such as LPSC, between $Li_{1.75}ZrCl_{4.75}O_{0.5}$ and the Li metal anode remains crucial to alleviate severe interfacial side reactions and guarantee stable electrochemical performance. In addition, the $LaCl_3$-based SSE developed by Yin *et al.*, $Li_{0.388}Ta_{0.238}La_{0.475}Cl_3$, could achieve close contact with the Li metal anode. At a current density of 1 mA h cm^{-2}, the lithium symmetric battery could maintain stability for over 5000 hours (Fig. 10f), primarily due to the formation of a gradient insulating passivation layer composed of electron-insulating LiCl at the interface, which promoted uniform Li plating/stripping behavior (Fig. 10g). In particular, the dense nanocrystalline characteristics of $Li_{0.388}Ta_{0.238}La_{0.475}Cl_3$ also contributed to enhancing the SSE/Li interfacial stability, as demonstrated by the close contact between $Li_{0.388}Ta_{0.238}La_{0.475}Cl_3$ and the Li metal anode, which persisted even after 50 hours of cycling (Fig. 10h).

4.3 Stability of halide SSEs towards high-voltage cathodes

Although most halide SSEs display high oxidation potentials (>4 V *vs.* Li^+/Li), they are still insufficient to directly match some high-voltage Ni-rich layered $LiMO_2$ (M = Ni, Co, Mn, and Al) cathodes. In the case of Cl-based halides, Cl^- is oxidized to form the Li-deficient metal chloride MCl_3 above 4.3 V.[66] In particular, when Li_3InCl_6 comes into contact with high-capacity $Li_{1.15}Mn_{0.53}Ni_{0.265}Co_{0.055}O_2$ (LRM), the Li_3InCl_6 suffers a severe oxidation reaction to form In_2O_3 at a high voltage of 4.8 V.[147] These Li-deficient metal compounds block the Li^+ transport path in the composite cathode and continuously decompose the SSE, thus deteriorating the cycling stability of the ASSLBs. Hence, the search for SSEs with both high-voltage stability and high ionic conductivity is crucial for the construction of high energy density ASSLBs.

The F-based halide is predicted to have the oxidation potential of more than 6 V, so the oxidation reaction under high voltage can be inhibited by *in situ* formation of F-rich CEI at the cathode/SSEs interface (Fig. 11a). A dual-halogen SSE, $Li_3InCl_{4.8}F_{1.2}$, was developed by Zhang *et al.*[28] Compared with the Li_3InCl_6, the ASSLB with bare $LiCoO_2$ and $Li_3InCl_{4.8}F_{1.2}$ could deliver higher reversible capacity (203.7 mAh g^{-1}) and initial coulombic efficiency (89.2%) at a cut-off voltage of 4.8 V (Fig. 11c). According to the first principles computation result, this stemmed from the generation of F-containing compounds (including LiF, $LiInF_4$, and InF_3) after $Li_3InCl_{4.8}F_{1.2}$ exceeded the theoretical oxidation limit of 4.42 V (Fig. 11b), which

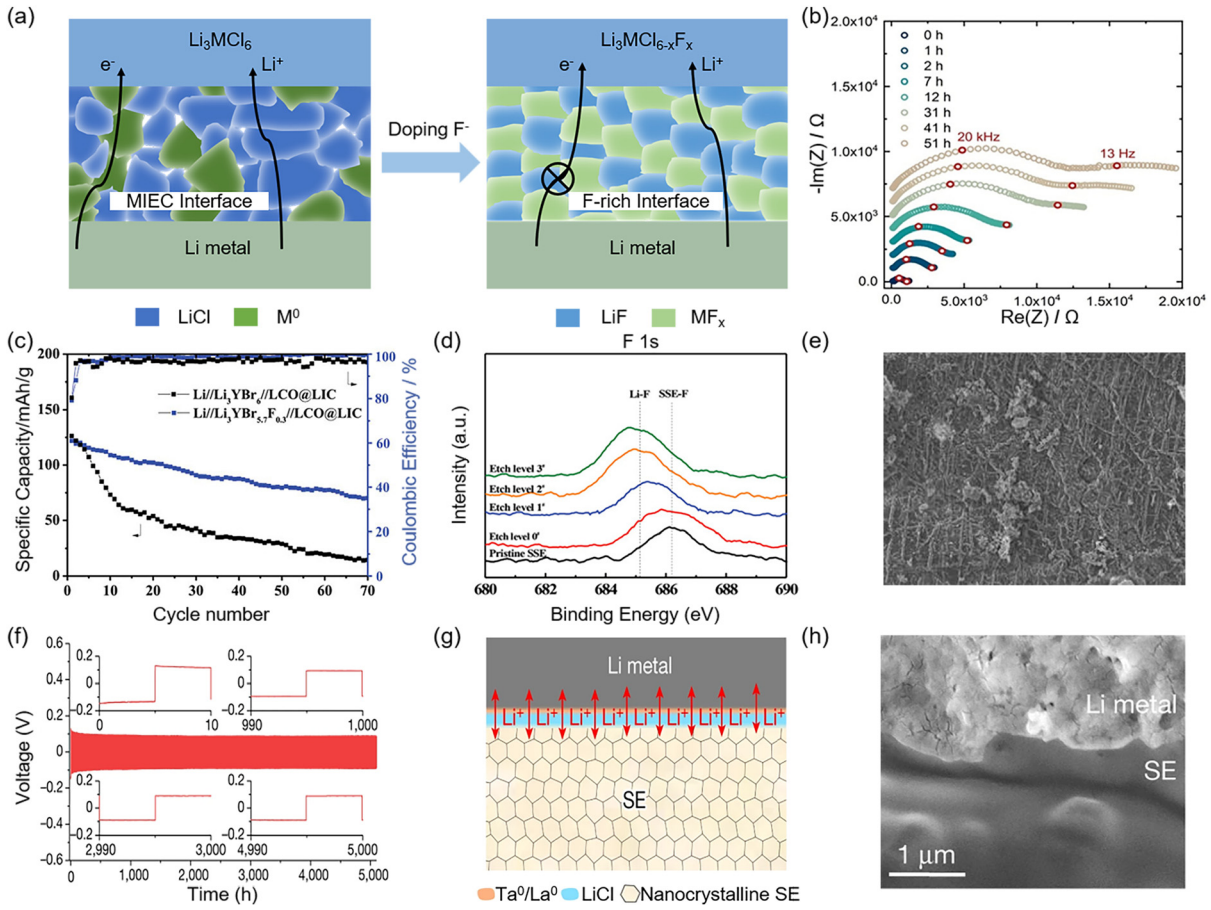

Fig. 10 Stability between halide SSEs and Li metal anode. (a) Interfacial comparison of Li_3MCl_6 and $Li_3MCl_{6-x}F_x$ in contact with Li metal anode. (b) Evolution of interfacial impedance with time extension of Li//Li_3InCl_6//Li symmetric battery. Reproduced with permissions from ref. 135. Copyright 2020, Wiley-VCH. (c) Cycling stability for Li//$Li_3YBr_{5.7}F_{0.3}$//LCO@LIC battery. (d) Overall XPS spectra evolution of F 1s at the $Li_3YBr_{5.7}F_{0.3}$/Li interface under different etch levels. (e) SEM of the Li metal anode surface morphology after cycling 1000 h with $Li_3YBr_{5.7}F_{0.3}$ SSE direct matching. Reproduced with permissions from ref. 136. Copyright 2021, Wiley-VCH. (f) Li plating/stripping voltage profiles for Li//$Li_{0.388}Ta_{0.238}La_{0.475}Cl_3$//Li symmetric battery. (g) Schematic of the gradient insulation passivation layer. The red double arrows represent Li^+ fluxes. (h) Cross-sectional SEM of Li/$Li_{0.388}Ta_{0.238}La_{0.475}Cl_3$/Li metal interface after cycling 50 h. Reproduced with permissions from ref. 32. Copyright 2023, Springer Nature.

formed a passivated interphase that prevented the SSE from further decomposition. This was further confirmed by the F K-edge XAS spectra of the cycled LCO/SSE composite cathodes, both of which exhibited a high-energy shift compared with the pristine SSE and a low-energy shift in absorption edges compared with standard LiF (Fig. 11d). This implied the formation of a LiF-rich passivating cathode-electrolyte interphase (CEI) after the first cycle, and subsequent scanning transmission X-ray microscopy (STXM) mapping of a single cycled LCO particle also showed a uniform distribution of F on the surface (Fig. 11e).

Similarly, Shen *et al.* succeeded in raising the practical oxidation limit of Li_2ZrCl_6 to 4.87 V with excellent ionic conductivity (~1.13×10^{-3} S cm^{-1}) by employing the F^-/O^{2-} co-doping strategy.[139] The TEM image of the cycled NCM with LZCFO, shown in Fig. 11f, indicated that a flat CEI layer was uniformly generated on the surface, covering the particle, which was responsible for the enhanced oxidation stability. The chemical composition of the CEI layer for the cycled composite cathode was further revealed by ToF-SIMS and XPS (Fig. 11g). The concentration of ClO_x^- for the cycled NCM with LZCFO was significantly lower, demonstrating that the decomposition of the SSE was effectively inhibited by the formation of the F-rich CEI. Surprisingly, unlike F^- doping, the mixed metal–chlorine spinel halide $Li_2In_{1/3}Sc_{1/3}Cl_4$ prepared by Zhou *et al.* was able to achieve stable cycling at a cut-off voltage of 4.8 V when matched with bare NCM85 (Fig. 11i).[30] It was benefited by the low electronic conductivity of $Li_2In_{1/3}Sc_{1/3}Cl_4$ (4.7×10^{-10} S cm^{-1}) leading to minimal reaction with NCM85. In addition, related studies have suggested that the oxidation stability of halide SSEs may also be related to the stability degree of the valence electron structure for the central metal element. As described by Xu *et al.*, Li_3YbCl_6 exhibits good oxidation stability at over 4.5 V due to the fully occupied atomic orbitals of Yb, suggesting that Yb^{3+} has the potential to enhance the high-voltage stability of halide SSEs.[60]

In summary, chemical substitution has been shown to broaden the intrinsic electrochemical window of halide SSEs,

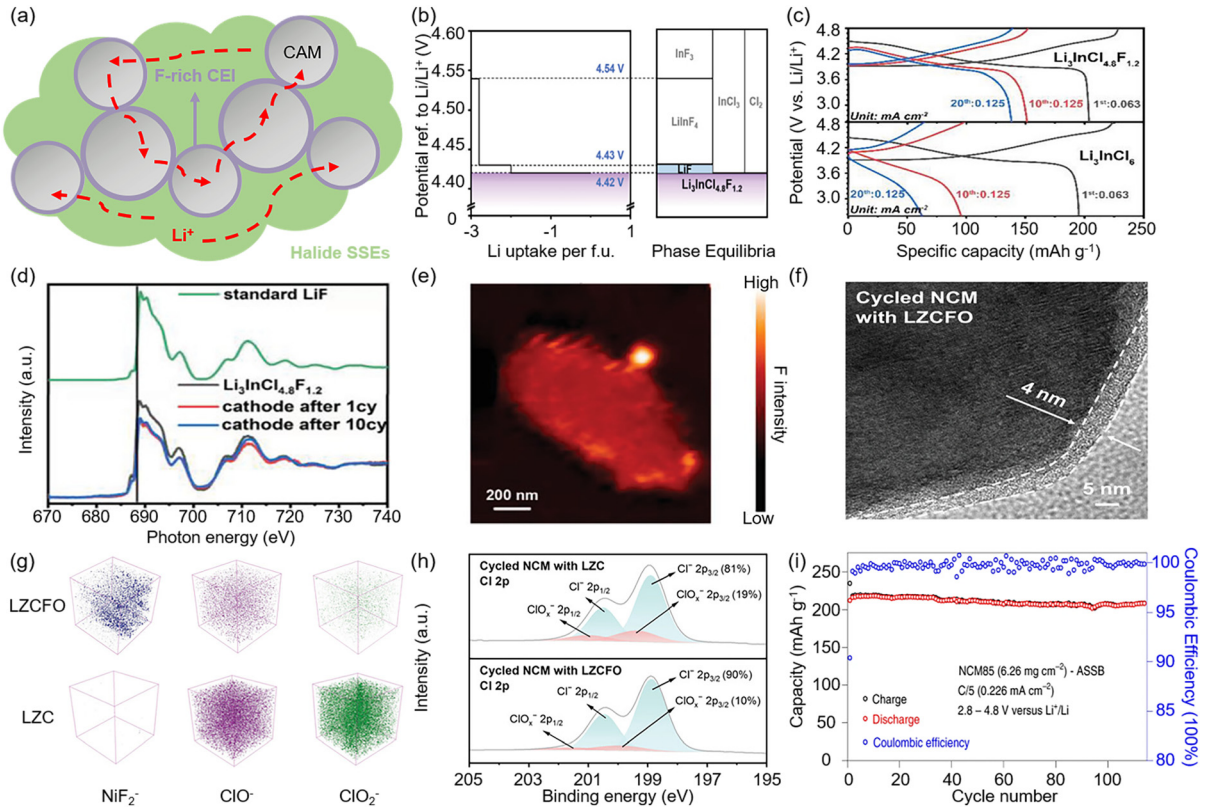

Fig. 11 Stability between halide SSEs and high-voltage cathode. (a) Formation of F-rich CEI prevents blockage of Li^+ conduction path in composite cathode. (b) Calculated phase equilibria of $Li_3InCl_{4.8}F_{1.2}$ at varous Li^+/Li potentials. (c) Charge–discharge voltage profiles comparison of different cathode SSE batteries in the voltage range of 2.6–4.8 V. (d) F K-edge XAS spectra of the cycled LCO/SSE composite cathodes. (e) STXM mapping image of a single cycled LCO particle. Reproduced with permissions from ref. 28. Copyright 2021, Wiley-VCH. (f) TEM image of cycled NCM with LZCFO. (g) Comparison of NiF_2^-, ClO^-, ClO_2^- content in cyclic NCM with LZCFO and LZC from ToF-SIMS. (h) Difference in ClO_x^- content from the deconvoluted Cl 2p XPS spectrum. Reproduced with permissions from ref. 139. Copyright 2024, Wiley-VCH. (i) Long-term cycling of the NCM85 ASSB with $Li_2In_{1/3}Sc_{1/3}Cl_4$ between 2.8 V and 4.8 V. Reproduced with permissions from ref. 30. Copyright 2022, Springer Nature.

making an important contribution for driving the high energy density of halide-based ASSLBs.

5. Summary and outlook

As opposed to other types of SSEs, it is the intrinsic characteristics of halide SSEs that have enabled them to become the potential stock for the energy storage field of high-performance ASSLBs in recent years. The first is that the lower valence of halogen ions gives the halide SSEs weaker bond cooperation against Li^+, resulting in lower energy barrier migration for Li^+ in the skeleton structure. Secondly, the larger ionic radii and higher polarizability of halogen ions facilitate the formation of wider Li^+ transport channels and higher ion mobility, which ultimately enables halide SSEs to display excellent ion transport kinetics and good deformability. Even the stringent requirements of ASSLBs for the assembly environment are reduced due to the stronger stability of halide SSEs in air/humidity.

In this review, starting from the structural framework and ionic conduction mechanism, the basic concepts of halide SSEs were discussed and the implications of anion polarizability, cation disorder and stacking faults on Li-ion migration were specifically analyzed. Immediately thereafter, the common substitution types were summarized and it was shown that optimized crystal structures and Li^+ migration kinetics can be obtained by selecting suitable substituent elements and contents for the chemical modification of halide SSEs. In addition, the mechanism of severe interfacial reactions between halide SSEs and high-voltage cathodes or Li metal anode has been revealed, and the strategy of inhibiting interfacial side reaction by using chemical substitution has been proposed to achieve excellent electrochemical compatibility with common electrodes. Although halide SSEs have made impressive achievements in just a few years, shortcomings caused by the physicochemical nature of halogen ions still prevent them from being commercially promoted. Some potential future research directions are as follows:

(1) In-depth exploration of the relationship between local structure evolution and ion transport. Currently, the RT ionic conductivity of most halide SSEs has not yet reached 10^{-3} S cm^{-1}; in particular, the development of fluoride SSEs is seriously limited, with the maximum of only 10^{-5} S cm^{-1}, which is far from the theoretically calculated value. The ionic

conductivity of halide SSEs is related to their overall/local structure, so it is necessary to have a comprehensive and thorough understanding of the crystal structure and ion migration path of halide SSEs, with the focus on how the local structural evolution shapes the ion transport behavior in halide SSEs. In addition, while amorphous halide SSEs demonstrate great potential in terms of reducing ion migration barrier, the role played by amorphous degree in achieving high ionic conductivity remains unclear, necessitating further exploration into their formation mechanisms. The mechanical knowledge of structure–property relationships can provide materials design principles for engineering strategies such as regulating the trade-off between vacancy concentration and Li^+ content, modulating cation disorder and optimizing synthesis parameters, ultimately giving rise to the quantum leap in the ionic conductivity of halide SSEs.

(2) Advanced theoretical calculations can guide the discovery of novel halide SSEs with excellent ionic conductivity and electrochemical stability. Boosting the ion transport performance of halide SSEs through elemental substitution has been widely recognized as an effective tool, but the consideration of substitution elements for ternary halide SSEs has traditionally been obtained through a large number of experimental studies, which is both time-consuming and labor-intensive. With the development of computer technology, the advent of high-throughput simulation helps to quickly screen and identify appropriate substituent ions and content, which greatly elevates the efficiency of preliminary experiments and shortens the experiment period. In addition, advanced computational methods, including AIMD and DFT, can be used to evaluate the chemical/electrochemical stability of halide SSEs, which in turn can be used to select mild operating conditions and high specific energy electrode materials for matching.

(3) *In situ*/operational observation of interface problems using fine characterization techniques. The degree of interfacial reaction between ASSLBs components is so important that it can determine the overall ion transport rate of ASSLBs. Yet, using conventional interfacial characterization techniques is difficult to accurately reflect the dynamic evolution of the charge/discharge process, which makes the exploration of the interfacial problems always ambiguous. Therefore, there is an urgent need for high-precision characterization techniques, such as transmission X-ray microscopy and X-ray computed tomography, to continuously monitor the interfacial contact between components at high resolution without damaging the interface. And the theoretical model established with the aid of computational simulation can provide clear insight into the structure and function of various surfaces, so as to better guide the formulation of strategies for improving the interfacial stability.

To conclude, only by combining advanced theoretical calculation and characterization methods to clarify the basic research content of structure and composition can we promote the commercialization progress of halide SSEs in high energy density ASSLBs, and better satisfy the wide temperature range and long lifetime required in practical working conditions.

Data availability

No primary research results, software or code have been included and no new data were generated or analysed as part of this review.

Conflicts of interest

There are no conflicts of interest to declare.

Acknowledgements

We gratefully acknowledge support from the National Key R&D Program of China (2021YFB2400400, 2022YFB2404600), the National Natural Science Foundation of China (Grant No. 22379120), the Key Research and Development Plan of Shanxi Province (China, Grant No. 2021JLM-36), "Young Talent Support Plan" of Xi'an Jiaotong University (71211201010723), "Young Talent Support Plan" of Xi'an Jiaotong University (HG6J003), "1000-Plan program" of Shaanxi Province and the Higher Education Institution Academic Discipline Innovation and Talent Introduction Plan ("111 Plan") (No. B23025).

References

1 A. Manthiram, X. Yu and S. Wang, *Nat. Rev. Mater.*, 2017, **2**, 16103.
2 C. Sun, J. Liu, Y. Gong, D. P. Wilkinson and J. Zhang, *Nano Energy*, 2017, **33**, 363–386.
3 Q. Zhao, S. Stalin, C.-Z. Zhao and L. A. Archer, *Nat. Rev. Mater.*, 2020, **5**, 229–252.
4 L. Zhao, A. E. Lakraychi, Z. Chen, Y. Liang and Y. Yao, *ACS Energy Lett.*, 2021, **6**, 3287–3306.
5 H. Jamal, F. Khan, S. Hyun, S. W. Min and J. H. Kim, *J. Mater. Chem. A*, 2021, **9**, 4126–4137.
6 H. Jamal, F. Khan, H.-R. Si and J. H. Kim, *J. Mater. Chem. A*, 2021, **9**, 27304–27319.
7 E. Kim, H. Jamal, I. Jeon, F. Khan, S.-E. Chun and J. H. Kim, *Adv. Energy Mater.*, 2023, **13**, 2301674.
8 Z. Li, J. Fu, X. Zhou, S. Gui, L. Wei, H. Yang, H. Li and X. Guo, *Adv. Sci.*, 2023, **10**, 2201718.
9 J. Tan, Z. Wang, J. Cui, Z. Jia, W. Tian, C. Wu, C. Peng, C. Shu, K. Yang and W. Tang, *J. Energy Chem.*, 2024, **95**, 288–295.
10 K. J. Kim, M. Balaish, M. Wadaguchi, L. Kong and J. L. M. Rupp, *Adv. Energy Mater.*, 2021, **11**, 2002689.
11 Z. Jia, H. Shen, J. Kou, T. Zhang, Z. Wang, W. Tang, M. Doeff, C.-Y. Chiang and K. Chen, *Adv. Mater.*, 2024, **36**, 2309019.
12 Q. Zhang, D. Cao, Y. Ma, A. Natan, P. Aurora and H. Zhu, *Adv. Mater.*, 2019, **31**, 1901131.
13 J. Wu, S. Liu, F. Han, X. Yao and C. Wang, *Adv. Mater.*, 2021, **33**, 2000751.

14 C. Wang, J. Liang, Y. Zhao, M. Zheng, X. Li and X. Sun, *Energy Environ. Sci.*, 2021, **14**, 2577–2619.
15 X. Li, J. Liang, X. Yang, K. R. Adair, C. Wang, F. Zhao and X. Sun, *Energy Environ. Sci.*, 2020, **13**, 1429–1461.
16 H. Kwak, S. Wang, J. Park, Y. Liu, K. T. Kim, Y. Choi, Y. Mo and Y. S. Jung, *ACS Energy Lett.*, 2022, **7**, 1776–1805.
17 K. Tuo, C. Sun and S. Liu, *Electrochem. Energy Rev.*, 2023, **6**, 17.
18 D. C. Ginnings and T. E. Phipps, *J. Am. Chem. Soc.*, 1930, **52**, 1340–1345.
19 C. C. Liang, J. Epstein and G. H. Boyle, *J. Electrochem. Soc.*, 1969, **116**, 1452.
20 A. Bohnsack, G. Balzer, M. S. Wickleder, H.-U. Güdel and G. Meyer, *Z. Anorg. Allg. Chem.*, 1997, **623**, 1352–1356.
21 Y. Tomita, H. Matsushita, K. Kobayashi, Y. Maeda and K. Yamada, *Solid State Ionics*, 2008, **179**, 867–870.
22 T. Asano, A. Sakai, S. Ouchi, M. Sakaida, A. Miyazaki and S. Hasegawa, *Adv. Mater.*, 2018, **30**, 1803075.
23 X. Li, J. Liang, N. Chen, J. Luo, K. R. Adair, C. Wang, M. N. Banis, T. Sham, L. Zhang, S. Zhao, S. Lu, H. Huang, R. Li and X. Sun, *Angew. Chem., Int. Ed.*, 2019, **58**, 16427–16432.
24 R. Schlem, S. Muy, N. Prinz, A. Banik, Y. Shao-Horn, M. Zobel and W. G. Zeier, *Adv. Energy Mater.*, 2020, **10**, 1903719.
25 R. Schlem, T. Bernges, C. Li, M. A. Kraft, N. Minafra and W. G. Zeier, *ACS Appl. Energy Mater.*, 2020, **3**, 3684–3691.
26 K.-H. Park, K. Kaup, A. Assoud, Q. Zhang, X. Wu and L. F. Nazar, *ACS Energy Lett.*, 2020, **5**, 533–539.
27 C. Wang, J. Liang, J. Luo, J. Liu, X. Li, F. Zhao, R. Li, H. Huang, S. Zhao, L. Zhang, J. Wang and X. Sun, *Sci. Adv.*, 2021, **7**, eabh1896.
28 S. Zhang, F. Zhao, S. Wang, J. Liang, J. Wang, C. Wang, H. Zhang, K. Adair, W. Li, M. Li, H. Duan, Y. Zhao, R. Yu, R. Li, H. Huang, L. Zhang, S. Zhao, S. Lu, T.-K. Sham, Y. Mo and X. Sun, *Adv. Energy Mater.*, 2021, **11**, 2100836.
29 Z. Liu, S. Ma, J. Liu, S. Xiong, Y. Ma and H. Chen, *ACS Energy Lett.*, 2021, **6**, 298–304.
30 L. Zhou, T.-T. Zuo, C. Y. Kwok, S. Y. Kim, A. Assoud, Q. Zhang, J. Janek and L. F. Nazar, *Nat. Energy*, 2022, **7**, 83–93.
31 E. Sebti, H. A. Evans, H. Chen, P. M. Richardson, K. M. White, R. Giovine, K. P. Koirala, Y. Xu, E. Gonzalez-Correa, C. Wang, C. M. Brown, A. K. Cheetham, P. Canepa and R. J. Clément, *J. Am. Chem. Soc.*, 2022, **144**, 5795–5811.
32 Y.-C. Yin, J.-T. Yang, J.-D. Luo, G.-X. Lu, Z. Huang, J.-P. Wang, P. Li, F. Li, Y.-C. Wu, T. Tian, Y.-F. Meng, H.-S. Mo, Y.-H. Song, J.-N. Yang, L.-Z. Feng, T. Ma, W. Wen, K. Gong, L.-J. Wang, H.-X. Ju, Y. Xiao, Z. Li, X. Tao and H.-B. Yao, *Nature*, 2023, **616**, 77–83.
33 W. Li, M. Li, P.-H. Chien, S. Wang, C. Yu, G. King, Y. Hu, Q. Xiao, M. Shakouri, R. Feng, B. Fu, H. Abdolvand, A. Fraser, R. Li, Y. Huang, J. Liu, Y. Mo, T.-K. Sham and X. Sun, *Sci. Adv.*, 2023, **9**, eadh4626.
34 S. Zhang, F. Zhao, L.-Y. Chang, Y.-C. Chuang, Z. Zhang, Y. Zhu, X. Hao, J. Fu, J. Chen, J. Luo, M. Li, Y. Gao, Y. Huang, T.-K. Sham, M. D. Gu, Y. Zhang, G. King and X. Sun, *J. Am. Chem. Soc.*, 2024, **146**, 2977–2985.
35 B. Hong, L. Gao, P. Nan, Y. Li, M. Liu, R. Zou, J. Gu, Q. Xu, J. Zhu and S. Han, *Angew. Chem., Int. Ed.*, 2024, e202415847.
36 J. Hu, K. Chen and C. Li, *ACS Appl. Mater. Interfaces*, 2018, **10**, 34322–34331.
37 J. Hu, Z. Yao, K. Chen and C. Li, *Energy Storage Mater.*, 2020, **28**, 37–46.
38 X. Li, J. Liang, J. Luo, M. Norouzi Banis, C. Wang, W. Li, S. Deng, C. Yu, F. Zhao, Y. Hu, T.-K. Sham, L. Zhang, S. Zhao, S. Lu, H. Huang, R. Li, K. R. Adair and X. Sun, *Energy Environ. Sci.*, 2019, **12**, 2665–2671.
39 J. Liang, X. Li, S. Wang, K. R. Adair, W. Li, Y. Zhao, C. Wang, Y. Hu, L. Zhang, S. Zhao, S. Lu, H. Huang, R. Li, Y. Mo and X. Sun, *J. Am. Chem. Soc.*, 2020, **142**, 7012–7022.
40 S. Muy, J. Voss, R. Schlem, R. Koerver, S. J. Sedlmaier, F. Maglia, P. Lamp, W. G. Zeier and Y. Shao-Horn, *iScience*, 2019, **16**, 270–282.
41 L. Zhou, C. Y. Kwok, A. Shyamsunder, Q. Zhang, X. Wu and L. F. Nazar, *Energy Environ. Sci.*, 2020, **13**, 2056–2063.
42 X. Shi, Z. Zeng, M. Sun, B. Huang, H. Zhang, W. Luo, Y. Huang, Y. Du and C. Yan, *Nano Lett.*, 2021, **21**, 9325–9331.
43 H. Kwak, D. Han, J. Lyoo, J. Park, S. H. Jung, Y. Han, G. Kwon, H. Kim, S.-T. Hong, K.-W. Nam and Y. S. Jung, *Adv. Energy Mater.*, 2021, **11**, 2003190.
44 X. Li, J. Liang, K. R. Adair, J. Li, W. Li, F. Zhao, Y. Hu, T.-K. Sham, L. Zhang, S. Zhao, S. Lu, H. Huang, R. Li, N. Chen and X. Sun, *Nano Lett.*, 2020, **20**, 4384–4392.
45 F. Liu, L. Gao, Z. Zhang, L. Zhang, N. Deng, Y. Zhao and W. Kang, *Energy Storage Mater.*, 2024, **64**, 103072.
46 L. Guo, J. Zheng, L. Zhao and Y. Yao, *MRS Bull.*, 2023, **48**, 1247–1256.
47 C. Zhang, H. Zhuang, Z. Qi, X. Liu and Y. Ren, *Mater. Today Commun.*, 2023, **35**, 105764.
48 H. Liu, D. Li, C. Dong, Y. Li, H. Yuan, D. Yu, L. Gao, P. Ding, Y. Li, Z. Qin, Y. Liang, H. Luo, L. Li, Y. Ren, L. Fan and C. Nan, *Adv. Energy Mater.*, 2024, **14**, 2402064.
49 D. Lee, Z. Cui, J. B. Goodenough and A. Manthiram, *Small*, 2024, **20**, 2306053.
50 C. Wang, X. Li, Y. Zhao, M. N. Banis, J. Liang, X. Li, Y. Sun, K. R. Adair, Q. Sun, Y. Liu, F. Zhao, S. Deng, X. Lin, R. Li, Y. Hu, T. Sham, H. Huang, L. Zhang, R. Yang, S. Lu and X. Sun, *Small Methods*, 2019, **3**, 1900261.
51 Y. Shi, Q. Li, X. Hu, Y. Liao, W. Li, Y. Xu, B. Zhao, J. Zhang and Y. Jiang, *Nano Energy*, 2024, **120**, 109150.
52 T. Duan, H. Cheng, Y. Liu, Q. Sun, W. Nie, X. Lu, P. Dong and M.-K. Song, *Energy Storage Mater.*, 2024, **65**, 103091.
53 Y.-C. Lan, P.-H. Lai, B. D. Vogt and E. D. Gomez, *ACS Energy Lett.*, 2024, **9**, 3324–3334.

54 X. Shi, Z. Zeng, H. Zhang, B. Huang, M. Sun, H. H. Wong, Q. Lu, W. Luo, Y. Huang, Y. Du and C.-H. Yan, *Small Methods*, 2021, **5**, 2101002.
55 X. Luo, D. Cai, X. Wang, X. Xia, C. Gu and J. Tu, *ACS Appl. Mater. Interfaces*, 2022, **14**, 29844–29855.
56 T. Ma, Z. Wang, D. Wu, P. Lu, X. Zhu, M. Yang, J. Peng, L. Chen, H. Li and F. Wu, *Energy Environ. Sci.*, 2023, **16**, 2142–2152.
57 J. Liang, X. Li, K. R. Adair and X. Sun, *Acc. Chem. Res.*, 2021, **54**, 1023–1033.
58 C. Wang, J. Liang, J. T. Kim and X. Sun, *Sci. Adv.*, 2022, **8**, eadc9516.
59 J. Park, D. Han, H. Kwak, Y. Han, Y. J. Choi, K.-W. Nam and Y. S. Jung, *Chem. Eng. J.*, 2021, **425**, 130630.
60 G. Xu, L. Luo, J. Liang, S. Zhao, R. Yang, C. Wang, T. Yu, L. Wang, W. Xiao, J. Wang, J. Yu and X. Sun, *Nano Energy*, 2022, **92**, 106674.
61 J. Pan, L. Gao, X. Zhang, D. Huang, J. Zhu, L. Wang, Y. Wei, W. Yin, Y. Xia, R. Zou, Y. Zhao and S. Han, *Inorg. Chem.*, 2024, **63**, 3418–3427.
62 J. Fu, S. Wang, J. Liang, S. H. Alahakoon, D. Wu, J. Luo, H. Duan, S. Zhang, F. Zhao, W. Li, M. Li, X. Hao, X. Li, J. Chen, N. Chen, G. King, L.-Y. Chang, R. Li, Y. Huang, M. Gu, T.-K. Sham, Y. Mo and X. Sun, *J. Am. Chem. Soc.*, 2023, **145**, 2183–2194.
63 J.-D. Luo, Y. Zhang, X. Cheng, F. Li, H.-Y. Tan, M.-Y. Zhou, Z.-W. Wang, X.-D. Hao, Y.-C. Yin, B. Jiang and H.-B. Yao, *Angew. Chem., Int. Ed.*, 2024, **63**, e202400424.
64 X. Hao, K. Chen, M. Jiang, Y. Tang, Y. Liu and K. Cai, *J. Mater. Chem. A*, 2024, **12**, 18459–18468.
65 K. Chen, X. Hao, M. Jiang and Y. Tang, *J. Alloys Compd.*, 2024, **997**, 174945.
66 S. Wang, Q. Bai, A. M. Nolan, Y. Liu, S. Gong, Q. Sun and Y. Mo, *Angew. Chem., Int. Ed.*, 2019, **58**, 8039–8043.
67 S. R. Combs, P. K. Todd, P. Gorai and A. E. Maughan, *J. Electrochem. Soc.*, 2022, **169**, 040551.
68 T. Famprikis, P. Canepa, J. A. Dawson, M. S. Islam and C. Masquelier, *Nat. Mater.*, 2019, **18**, 1278–1291.
69 A. Van Der Ven, J. Bhattacharya and A. A. Belak, *Acc. Chem. Res.*, 2013, **46**, 1216–1225.
70 B. He, F. Zhang, Y. Xin, C. Xu, X. Hu, X. Wu, Y. Yang and H. Tian, *Nat. Rev. Chem.*, 2023, **7**, 826–842.
71 G. Yang, X. Liang, S. Zheng, H. Chen, W. Zhang, S. Li and F. Pan, *eScience*, 2022, **2**, 79–86.
72 Y. Liu, S. Wang, A. M. Nolan, C. Ling and Y. Mo, *Adv. Energy Mater.*, 2020, **10**, 2002356.
73 R. Kanno and M. Murayama, *J. Electrochem. Soc.*, 2001, **148**, A742.
74 Z. Xu, X. Chen, K. Liu, R. Chen, X. Zeng and H. Zhu, *Chem. Mater.*, 2019, **31**, 7425–7433.
75 N. Flores-González, M. López, N. Minafra, J. Bohnenberger, F. Viñes, S. Rudić, I. Krossing, W. G. Zeier, F. Illas and D. H. Gregory, *J. Mater. Chem. A*, 2022, **10**, 13467–13475.
76 S. Muy, J. C. Bachman, L. Giordano, H.-H. Chang, D. L. Abernathy, D. Bansal, O. Delaire, S. Hori, R. Kanno, F. Maglia, S. Lupart, P. Lamp and Y. Shao-Horn, *Energy Environ. Sci.*, 2018, **11**, 850–859.
77 R. Schlem, A. Banik, S. Ohno, E. Suard and W. G. Zeier, *Chem. Mater.*, 2021, **33**, 327–337.
78 B. Helm, R. Schlem, B. Wankmiller, A. Banik, A. Gautam, J. Ruhl, C. Li, M. R. Hansen and W. G. Zeier, *Chem. Mater.*, 2021, **33**, 4773–4782.
79 H. Ito, K. Shitara, Y. Wang, K. Fujii, M. Yashima, Y. Goto, C. Moriyoshi, N. C. Rosero-Navarro, A. Miura and K. Tadanaga, *Adv. Sci.*, 2021, **8**, 2101413.
80 M. A. Plass, S. Bette, R. E. Dinnebier and B. V. Lotsch, *Chem. Mater.*, 2022, **34**, 3227–3235.
81 M. A. Plass, S. Bette, N. Philipp, I. Moundrakovski, K. Küster, R. E. Dinnebier and B. V. Lotsch, *J. Mater. Chem. A*, 2023, **11**, 13027–13038.
82 H. J. Lee, B. Darminto, S. Narayanan, M. Diaz-Lopez, A. W. Xiao, Y. Chart, J. H. Lee, J. A. Dawson and M. Pasta, *J. Mater. Chem. A*, 2022, **10**, 11574–11586.
83 K. Tuo, C. Sun, C. A. López, M. T. Fernández-Díaz and J. A. Alonso, *J. Mater. Chem. A*, 2023, **11**, 15651–15662.
84 C. Wang, S. Wang, X. Liu, Y. Wu, R. Yu, H. Duan, J. T. Kim, H. Huang, J. Wang, Y. Mo and X. Sun, *Energy Environ. Sci.*, 2023, **16**, 5136–5143.
85 L. Zhou, T. Zuo, C. Li, Q. Zhang, J. Janek and L. F. Nazar, *ACS Energy Lett.*, 2023, **8**, 3102–3111.
86 J. Peng, L. Xian and L.-B. Kong, *Ionics*, 2023, **29**, 2657–2664.
87 X. Luo, X. Wu, J. Xiang, D. Cai, M. Li, X. Wang, X. Xia, C. Gu and J. Tu, *ACS Appl. Mater. Interfaces*, 2021, **13**, 47610–47618.
88 H. Wang, Y. Li, Y. Tang, D. Ye, T. He, H. Zhao and J. Zhang, *ACS Appl. Mater. Interfaces*, 2023, **15**, 5504–5511.
89 Y. Ye, J. Geng, D. Zuo, K. Niu, D. Chen, J. Lin, X. Chen, H. J. Woo, Y. Zhu and J. Wan, *ACS Nano*, 2024, **18**, 18368–18378.
90 Z. Song, T. Wang, H. Yang, W. H. Kan, Y. Chen, Q. Yu, L. Wang, Y. Zhang, Y. Dai, H. Chen, W. Yin, T. Honda, M. Avdeev, H. Xu, J. Ma, Y. Huang and W. Luo, *Nat. Commun.*, 2024, **15**, 1481.
91 D. Li, D. Yu, G. Zhang, A. Du, Z. Ye, Y. Jia, W. Hou, T. Xu, F. Li, S. Chi, Y. Zhu and C. Yang, *Angew. Chem., Int. Ed.*, 2024, e202419735.
92 W. Li, Z. Chen, Y. Chen, W. Duan, G. Liu, Y. Lv, H. Yang and L. Yao, *Chem. Eng. J.*, 2023, **455**, 140509.
93 R. Li, P. Lu, X. Liang, L. Liu, M. Avdeev, Z. Deng, S. Li, K. Xu, J. Feng, R. Si, F. Wu, Z. Zhang and Y.-S. Hu, *ACS Energy Lett.*, 2024, **9**, 1043–1052.
94 H. Kwak, D. Han, J. P. Son, J. S. Kim, J. Park, K.-W. Nam, H. Kim and Y. S. Jung, *Chem. Eng. J.*, 2022, **437**, 135413.
95 S. Chen, C. Yu, C. Wei, Z. Jiang, Z. Zhang, L. Peng, S. Cheng and J. Xie, *Energy Mater. Adv.*, 2023, **4**, 0019.
96 K.-N. Gao, F. Bai, Z. Sun and T. Zhang, *Energy Storage Mater.*, 2024, **70**, 103444.
97 H. Zhang, Z. Yu, H. Chen, Y. Zhou, X. Huang and B. Tian, *J. Energy Chem.*, 2023, **79**, 348–356.

98 H.-J. Jeon, Y. Subramanian and K.-S. Ryu, *J. Power Sources*, 2024, **602**, 234343.
99 K.-H. Park, S. Y. Kim, M. Jung, S.-B. Lee, M.-J. Kim, I.-J. Yang, J.-H. Hwang, W. Cho, G. Chen, K. Kim and J. Yu, *ACS Appl. Mater. Interfaces*, 2023, **15**, 58367–58376.
100 J. Cheng, H. Zhang, Z. Wang, Y. Zhou, K. Yu, Y. Cheng, Z. Yu, X. Huang and B. Tian, *J. Energy Storage*, 2024, **89**, 111700.
101 E. Umeshbabu, S. Maddukuri, Y. Hu, M. Fichtner and A. R. Munnangi, *ACS Appl. Mater. Interfaces*, 2022, **14**, 25448–25456.
102 K. Tuo, F. Yin, F. Mi and C. Sun, *J. Energy Chem.*, 2023, **87**, 12–23.
103 S. Y. Kim, K. Kaup, K.-H. Park, A. Assoud, L. Zhou, J. Liu, X. Wu and L. F. Nazar, *ACS Mater. Lett.*, 2021, **3**, 930–938.
104 S. Yu, J. Noh, B. Kim, J.-H. Song, K. Oh, J. Yoo, S. Lee, S.-O. Park, W. Kim, B. Kang, D. Kil and K. Kang, *Science*, 2023, **382**, 573–579.
105 H. Zhang, Z. Zeng, X. Shi, C.-H. Wang and Y. Du, *EcoMat*, 2023, **5**, e12315.
106 J. Fu, S. Yang, J. Hou, L. Azhari, Z. Yao, X. Ma, Y. Liu, P. Vanaphuti, Z. Meng, Z. Yang, Y. Zhong and Y. Wang, *J. Power Sources*, 2023, **556**, 232465.
107 K. Wang, Q. Ren, Z. Gu, C. Duan, J. Wang, F. Zhu, Y. Fu, J. Hao, J. Zhu, L. He, C.-W. Wang, Y. Lu, J. Ma and C. Ma, *Nat. Commun.*, 2021, **12**, 4410.
108 F. Li, X. Cheng, L.-L. Lu, Y.-C. Yin, J.-D. Luo, G. Lu, Y.-F. Meng, H. Mo, T. Tian, J.-T. Yang, W. Wen, Z.-P. Liu, G. Zhang, C. Shang and H.-B. Yao, *Nano Lett.*, 2022, **22**, 2461–2469.
109 X. Luo, Y. Zhong, X. Wang, X. Xia, C. Gu and J. Tu, *ACS Appl. Mater. Interfaces*, 2022, **14**, 49839–49846.
110 T. H. Wan and F. Ciucci, *ACS Appl. Energy Mater.*, 2021, **4**, 7930–7941.
111 Y. Ren, J. Liu, C. Zhang, H. Zhuang, C. Sun, G. Cai, X. Tan and S. Sun, *Chem. Eng. J. Adv.*, 2022, **12**, 100377.
112 Y. Tomita, H. Nishiyama, K. Kobayashi, Y. Kohno, Y. Maeda and K. Yamada, *ECS Trans.*, 2009, **16**, 137.
113 T. Jeon and S. C. Jung, *J. Mater. Chem. A*, 2023, **11**, 4334–4344.
114 Y. Tanaka, K. Ueno, K. Mizuno, K. Takeuchi, T. Asano and A. Sakai, *Angew. Chem., Int. Ed.*, 2023, **62**, e202217581.
115 H. Kwak, J.-S. Kim, D. Han, J. S. Kim, J. Park, G. Kwon, S.-M. Bak, U. Heo, C. Park, H.-W. Lee, K.-W. Nam, D.-H. Seo and Y. S. Jung, *Nat. Commun.*, 2023, **14**, 2459.
116 L. Hu, J. Wang, K. Wang, Z. Gu, Z. Xi, H. Li, F. Chen, Y. Wang, Z. Li and C. Ma, *Nat. Commun.*, 2023, **14**, 3807.
117 S. Zhang, F. Zhao, J. Chen, J. Fu, J. Luo, S. H. Alahakoon, L.-Y. Chang, R. Feng, M. Shakouri, J. Liang, Y. Zhao, X. Li, L. He, Y. Huang, T.-K. Sham and X. Sun, *Nat. Commun.*, 2023, **14**, 3780.
118 G. Wang, S. Zhang, H. Wu, M. Zheng, C. Zhao, J. Liang, L. Zhou, J. Yue, X. Zhu, Y. Xu, N. Zhang, T. Pang, J. Fu, W. Li, Y. Xia, W. Yin, X. Sun and X. Li, *Adv. Mater.*, 2025, **37**, 2410402.
119 Y. Subramanian, R. Rajagopal and K.-S. Ryu, *ACS Appl. Mater. Interfaces*, 2024, **16**, 24534–24546.
120 X. Li, Y. Xu, C. Zhao, D. Wu, L. Wang, M. Zheng, X. Han, S. Zhang, J. Yue, B. Xiao, W. Xiao, L. Wang, T. Mei, M. Gu, J. Liang and X. Sun, *Angew. Chem., Int. Ed.*, 2023, **62**, e202306433.
121 W. D. Richards, L. J. Miara, Y. Wang, J. C. Kim and G. Ceder, *Chem. Mater.*, 2016, **28**, 266–273.
122 Z. Wang, J. Tan, Z. Jia, J. Cui, X. Wang, C. Shu, X. Gao, Y. Wu and W. Tang, *ACS Energy Lett.*, 2024, **9**, 4485–4492.
123 C. Wang, S. Hwang, M. Jiang, J. Liang, Y. Sun, K. Adair, M. Zheng, S. Mukherjee, X. Li, R. Li, H. Huang, S. Zhao, L. Zhang, S. Lu, J. Wang, C. V. Singh, D. Su and X. Sun, *Adv. Energy Mater.*, 2021, **11**, 2100210.
124 C. Wang, K. Adair and X. Sun, *Acc. Mater. Res.*, 2022, **3**, 21–32.
125 G. H. Chun, J. H. Shim and S. Yu, *ACS Appl. Mater. Interfaces*, 2022, **14**, 1241–1248.
126 W. Ji, D. Zheng, X. Zhang, T. Ding and D. Qu, *J. Mater. Chem. A*, 2021, **9**, 15012–15018.
127 X. Xu, G. Du, C. Cui, J. Liang, C. Zeng, S. Wang, Y. Ma and H. Li, *ACS Appl. Mater. Interfaces*, 2022, **14**, 39951–39958.
128 Z. Deng, Z. Jin, D. Chen, D. Ni, M. Tian, Y. Zhan, S. Li, Y. Sun, X. Huang and Y. Zhao, *ACS Appl. Mater. Interfaces*, 2022, **14**, 48619–48626.
129 H. Kobayashi, G. Yuan, Y. Gambe and I. Honma, *ACS Appl. Energy Mater.*, 2021, **4**, 9866–9870.
130 B. T. Tham, M.-S. Park, J. H. Kim and J. Moon, *J. Mater. Chem. A*, 2023, **11**, 15968–15978.
131 Y. Pang, J. Pan, J. Yang, S. Zheng and C. Wang, *Electrochem. Energy Rev.*, 2021, **4**, 169–193.
132 P. Minnmann, F. Strauss, A. Bielefeld, R. Ruess, P. Adelhelm, S. Burkhardt, S. L. Dreyer, E. Trevisanello, H. Ehrenberg, T. Brezesinski, F. H. Richter and J. Janek, *Adv. Energy Mater.*, 2022, **12**, 2201425.
133 J. Yun, H. R. Shin, T. D. Hoang, S. Kim, J. H. Choi, B. Kim, H. Jung, J. Moon and J.-W. Lee, *Energy Storage Mater.*, 2023, **59**, 102787.
134 Y. Fu and C. Ma, *Sci. China Mater.*, 2021, **64**, 1378–1385.
135 L. M. Riegger, R. Schlem, J. Sann, W. G. Zeier and J. Janek, *Angew. Chem., Int. Ed.*, 2021, **60**, 6718–6723.
136 T. Yu, J. Liang, L. Luo, L. Wang, F. Zhao, G. Xu, X. Bai, R. Yang, S. Zhao, J. Wang, J. Yu and X. Sun, *Adv. Energy Mater.*, 2021, **11**, 2101915.
137 K. Wang, Z. Gu, H. Liu, L. Hu, Y. Wu, J. Xu and C. Ma, *Adv. Sci.*, 2024, **11**, 2305394.
138 W. Tang, W. Xia, F. Hussain, J. Zhu, S. Han, W. Yin, P. Yu, J. Lei, D. S. Butenko, L. Wang and Y. Zhao, *J. Power Sources*, 2023, **568**, 232992.
139 L. Shen, J. Li, W. Kong, C. Bi, P. Xu, X. Huang, W. Huang, F. Fu, Y. Le, C. Zhao, H. Yuan, J. Huang and Q. Zhang, *Adv. Funct. Mater.*, 2024, **34**, 2408571.
140 Z. Li, L. Wang, X. Huang and X. He, *Small*, 2024, **20**, 2305429.
141 Y. Xiao, R. Xu, L. Xu, J.-F. Ding and J.-Q. Huang, *Energy Mater.*, 2021, **1**, 10013.

142 Z. Pan, H. Chen, Y. Zeng, Y. Ding, X. Pu and Z. Chen, *Energy Mater.*, 2023, **3**, 300054.
143 X. Chen, Z. Jia, H. Lv, C. Wang, N. Zhao and X. Guo, *J. Power Sources*, 2022, **545**, 231939.
144 X. Luo, X. He, H. Su, Y. Zhong, X. Wang and J. Tu, *Chem. Eng. J.*, 2023, **465**, 143036.
145 P. Ganesan, M. Soans, M. A. Cambaz, R. Zimmermanns, R. Gond, S. Fuchs, Y. Hu, S. Baumgart, M. Sotoudeh, D. Stepien, H. Stein, A. Groß, D. Bresser, A. Varzi and M. Fichtner, *ACS Appl. Mater. Interfaces*, 2023, **15**, 38391–38402.
146 Z. Zheng, H. Fang, Z. Liu and Y. Wang, *J. Electrochem. Soc.*, 2014, **162**, A244.
147 A. Zhang, J. Wang, R. Yu, H. Zhuo, C. Wang, Z. Ren and J. Wang, *ACS Appl. Mater. Interfaces*, 2023, **15**, 8190–8199.